Draft version June 23, 2020
Typeset using LaTeX **twocolumn** style in AASTeX63

Distinguishing between wet and dry atmospheres of TRAPPIST-1 e and f

Fabian Wunderlich [1,2,*] Markus Scheucher [1,2,*] M. Godolt [1] J. L. Grenfell [2] F. Schreier [3] P. C. Schneider [4] D. J. Wilson [5] A. Sánchez-López [6] M. López-Puertas [7] and H. Rauer [1,2,8]

[1] *Zentrum für Astronomie und Astrophysik, Technische Universität Berlin, 10623 Berlin, Germany*
[2] *Institut für Planetenforschung, Deutsches Zentrum für Luft- und Raumfahrt, 12489 Berlin, Germany*
[3] *Institut für Methodik der Fernerkundung, Deutsches Zentrum für Luft- und Raumfahrt, 82234 Oberpfaffenhofen, Germany*
[4] *Hamburger Sternwarte, Gojenbergsweg 112, 21029 Hamburg, Germany*
[5] *McDonald Observatory, University of Texas at Austin, Austin, TX 78712, USA*
[6] *Sterrewacht Leiden, Universiteit Leiden, Postbus 9513, 2300 RA Leiden, The Netherlands*
[7] *Instituto de Astrofísica de Andalucía (IAA-CSIC), Glorieta de la Astronoma s/n, 18008 Granada, Spain*
[8] *Institut für Geologische Wissenschaften, Freie Universität Berlin, 10623 Berlin, Germany*

(Received March 20, 2020; Revised May 26, 2020; Accepted June 11, 2020)

Submitted to ApJ

ABSTRACT

The nearby TRAPPIST-1 planetary system is an exciting target for characterizing the atmospheres of terrestrial planets. The planets e, f and g lie in the circumstellar habitable zone and could sustain liquid water on their surfaces. During the extended pre-main sequence phase of TRAPPIST-1, however, the planets may have experienced extreme water loss, leading to a desiccated mantle. The presence or absence of an ocean is challenging to determine with current and next generation telescopes. Therefore, we investigate whether indirect evidence of an ocean and/or a biosphere can be inferred from observations of the planetary atmosphere. We introduce a newly developed photochemical model for planetary atmospheres, coupled to a radiative-convective model and validate it against modern Earth, Venus and Mars. The coupled model is applied to the TRAPPIST-1 planets e and f, assuming different surface conditions and varying amounts of CO_2 in the atmosphere. As input for the model we use a constructed spectrum of TRAPPIST-1, based on near-simultaneous data from X-ray to optical wavelengths. We compute cloud-free transmission spectra of the planetary atmospheres and determine the detectability of molecular features using the Extremely Large Telescope (ELT) and the James Webb Space Telescope (JWST). We find that under certain conditions, the existence or non-existence of a biosphere and/or an ocean can be inferred by combining 30 transit observations with ELT and JWST within the K-band. A non-detection of CO could suggest the existence of an ocean, whereas significant CH_4 hints at the presence of a biosphere.

Keywords: planets and satellites: atmospheres - planets and satellites: detection - planets and satellites: individual (TRAPPIST-1) - planets and satellites: terrestrial planets

1. INTRODUCTION

The nearby TRAPPIST-1 system offers exciting new opportunities for studying the atmospheres of its seven planets with next generation telescopes such as the JWST (James Webb Space Telescope; Gardner et al. 2006; Beichman et al. 2014) or the ELT (European Large Telescope; Gilmozzi & Spyromilio 2007). Due to short orbital periods and large star-planet contrast ratios, planets orbiting such cool host stars are easier to detect and characterize via the transit method than planets orbiting hotter stars and are therefore prime targets to observe the properties of their atmospheres.

On the other hand the stellar luminosity evolution of M-dwarfs is quite different to that of solar-type stars. In

Corresponding author: Fabian Wunderlich
fabian.wunderlich@tu-berlin.de

* Equal Contribution Authors

particular the active pre-main sequence phase of the star can be extended and the stellar Ultra Violet (UV) radiation is high for about a billion years (see e.g. Baraffe et al. 2015; Luger & Barnes 2015). This could lead to a runaway greenhouse state on an ocean-bearing terrestrial planet and a loss of substantial amounts of planetary water vapour (H_2O) before the star enters the main sequence phase (see e.g. Wordsworth & Pierrehumbert 2013; Ramirez & Kaltenegger 2014; Luger & Barnes 2015; Tian & Ida 2015; Bolmont et al. 2016; Bourrier et al. 2017). Recently Fleming et al. (2020) suggest, that TRAPPIST-1 has maintained high activity with a saturated XUV luminosity (X-ray and extreme UV emission) for several Gyrs. Hence, the planets likely received a persistent and strong XUV flux from the host star for most of their lifetimes.

In such an environment with strong H_2O photolysis and subsequent hydrogen escape it has been suggested that the atmosphere could build up thousands of bar molecular oxygen (O_2) when assuming e.g. inefficient atmospheric loss or surface sinks (Wordsworth & Pierrehumbert 2014; Luger & Barnes 2015; Lincowski et al. 2018). This build-up can be prevented if O_2 is absorbed into the surface during the early magma ocean phase (see e.g. Schaefer et al. 2016; Wordsworth et al. 2018) or by extreme UV driven oxygen escape (Tian 2015; Dong et al. 2018; Guo 2019; Johnstone 2020). Grenfell et al. (2018) suggest, that if enough molecular hydrogen (H_2) is present it can react with O_2 from H_2O photolysis to reform water via explosion-combustion reactions.

Bolmont et al. (2016) concluded that the TRAPPIST-1 planets can retain significant amount of water even for strong far UV (FUV) photolysis of H_2O and large hydrogen escape rates. Three (TRAPPIST-1 e, f, and g) of the seven planets lie in the classical habitable zone (HZ), defined as the region around the star where a planet could maintain liquid water on its surface (Kasting et al. 1993). 3D simulations show that only TRAPPIST-1 e would allow for surface liquid water without the need of greenhouse warming from a gas other than H_2O (Wolf 2017; Turbet et al. 2018). The other two planets require greenhouse gases such as carbon dioxide (CO_2) and thick atmospheres to sustain surface habitability (Turbet et al. 2018).

The large FUV to near UV (NUV) stellar flux ratio of TRAPPIST-1 favors abiotic build-up of O_2 and O_3 in CO_2-rich atmospheres (e.g. Tian et al. 2014). Hence, O_2 or ozone (O_3) cannot be considered as reliable biosignature gases like on Earth (e.g. Selsis et al. 2002; Segura et al. 2007; Harman et al. 2015; Meadows 2017). Due to weak stellar UV emissions at wavelengths longer than 200 nm, planets orbiting M-stars show an increase in the abundance of certain bioindicators and biomarkers such as methane (CH_4) and nitrous oxide (N_2O) compared to the Earth around the Sun (see Segura et al. 2005; Rauer et al. 2011; Grenfell et al. 2013; Rugheimer et al. 2015; Wunderlich et al. 2019). Assuming the same surface emissions as on Earth, CH_4 would be detectable with the JWST in the atmosphere of a habitable zone Earth-like planet around TRAPPIST-1 (Wunderlich et al. 2019). Krissansen-Totton et al. (2018b) argued that the simultaneous detection of CH_4 and CO_2 in the atmosphere of a planet in the HZ is a potential biosignature. However, the build-up of detectable amounts of CH_4 is also conceivable by large outgassing from a more reducing mantle than Earth.

The detection of CO_2 in cloud-free atmospheres of TRAPPIST-1 planets would be feasible within approximately ten transits with the JWST (see Morley et al. 2017; Krissansen-Totton et al. 2018a; Wunderlich et al. 2019; Lustig-Yaeger et al. 2019; Fauchez et al. 2019; Komacek et al. 2020). The detection of other species, such as O_3 would require many more transits (see e.g. Lustig-Yaeger et al. 2019; Fauchez et al. 2019; Pidhorodetska et al. 2020). Another species which might be detectable in CO_2-rich atmospheres is carbon monoxide (CO), produced by CO_2 photolysis (e.g. Schwieterman et al. 2019). Since CO has only a few abiotic sinks and weak biogenic sources it is often considered as a potential antibiosignature (Zahnle et al. 2008; Wang et al. 2016; Nava-Sedeño et al. 2016; Meadows 2017; Catling et al. 2018).

Wang et al. (2016) argued that simultaneous observations of O_2 and CO would distinguish a true biosignature (O_2 without CO) from a photochemically produced false positive biosignature (O_2 with CO). However, Rodler & López-Morales (2014) showed that a detection of Earth-like O_2 levels with ELT would only be feasible for a planet around a late M-dwarf at a distance below ∼5 pc (see also Snellen et al. 2013; Brogi & Line 2019; Serindag & Snellen 2019).

In this study we investigate how the presence of an ocean as an efficient sink for CO would affect the atmospheric concentration of CO and other species. We simulate transmission spectra of TRAPPIST-1 e and TRAPPIST-1 f and determine the detectability of molecular features with the upcoming space-borne telescope JWST and the next generation ground-based telescope ELT. For the JWST we consider low resolution spectroscopy (LRS) and for the ELT we use high resolution spectroscopy (HRS). In particular we show how much CO_2 would be needed to obtain a detectable CO feature in a desiccated atmosphere of TRAPPIST-1 e.

Also the photochemical processes related to the existence of a water reservoir may change the abundances of

CO and O_2. The recombination of CO and atomic oxygen into CO_2 via catalytical cycles was suggested to be slower for dry CO_2 atmospheres due to the lower abundances of hydrogen oxides, HO_x (defined as H + OH + HO_2) (see e.g. Selsis et al. 2002; Segura et al. 2007; Krissansen-Totton et al. 2018b).

We use a 1D climate-photochemistry model to calculate the composition profiles of CO and other species such as O_2 and O_3 in CO_2-poor and CO_2-rich atmospheres. In order to consistently simulate the photochemical processes in CO_2-dominated atmospheres we introduced extensive model updates. The stellar Spectral Energy Distribution (SED) is an input for the model. The UV range of the SED is crucial for the photochemical processes in the atmosphere. To our knowledge we are the first study using an SED of TRAPPIST-1 constructed based on measurements in the UV (Wilson et al. submitted). For comparison we also investigate two other SEDs of TRAPPIST-1 with modelled or estimated UV fluxes as input for our climate-photochemistry model.

In Section 2 we introduce the climate-photochemistry model and validate the new version by calculating the atmospheres of modern Earth, Venus and Mars. We compare the results with other photochemical models and available observations. We also describe the line-by-line spectral model used to simulate transmission spectra of TRAPPIST-1 e and TRAPPIST-1 f, and introduce the calculation of the signal to noise ratio (S/N) of atmospheric molecular features. In Section 3 we show the TRAPPIST-1 SEDs used in this study and the considered atmospheric scenarios. Results of the atmospheric modelling, simulated transmission spectra and S/N calculations are presented in Section 4. In Section 5 we discuss our results and in Section 6 we present the summary and conclusion.

2. METHODOLOGY

2.1. *Climate-chemistry model*

To simulate the potential atmospheric conditions of the habitable zone planets TRAPPIST-1 e and TRAPPIST-1 f we use a 1D steady-state, cloud-free, radiative-convective photochemical model, entitled 1D-TERRA. The code is based on the model of Kasting & Ackerman (1986); Pavlov et al. (2000); Segura et al. (2003) and was further developed by e.g. von Paris et al. (2008, 2010); Rauer et al. (2011); von Paris et al. (2015); Gebauer et al. (2018b). We have extensively modified both the radiative-convective part of the model as well as the photochemistry module. The updated version of the model is capable of simulating a wide range of atmospheric temperatures (100 - 1000 K) and pressures (0.01 Pa - 10^3 bar). It covers a wide range of atmospheric compositions including potential habitable terrestrial planets, having N_2, CO_2, H_2 or H_2O-dominated atmospheres. The climate module is briefly described in Section 2.2. For a detailed description of the climate module we refer to the companion paper by Scheucher et al. (accepted). Here we give a detailed description of the updated photochemistry model in Section 2.3.

2.2. *Climate module*

The atmospheric temperature for each of the pressure layers is calculated with our climate module. The radiative transfer module REDFOX uses a flexible k-distribution model for opacity calculations based on the random-overlap assumption (see Scheucher et al. accepted). The radiative transfer is solved using the two-stream approximation (Toon et al. 1989). The module considers 20 absorbers from HITRAN 2016 (Gordon et al. 2017) as well as 81 absorbers in the visible (VIS) and ultraviolet (UV) with cross sections taken from the MPI Mainz Spectral Atlas (Keller-Rudek et al. 2013), the JPL Publication No. 15-10 (Burkholder et al. 2015), Mills (1998) and Zahnle et al. (2008).

Additionally, REDFOX includes Collision-Induced Absorption (CIA) data from HITRAN[1] and MT_CKD continua from Mlawer et al. (2012). Rayleigh scattering is considered using calculated cross sections of CO, CO_2, H_2O, N_2 and O_2 (Allen 1973) and measured cross sections of He, H_2 and CH_4 (Shardanand & Rao 1977).

To calculate the H_2O profile up to the cold trap we either use the relative humidity profile of the Earth taken from Manabe & Wetherald (1967) or we use a constant relative humidity throughout the troposphere. Above the cold trap the H_2O profile is calculated with the chemistry module. Godolt et al. (2016) showed that for surface temperatures warmer than the mean surface temperature of the Earth, the relative humidity profile of Manabe & Wetherald (1967) underestimates H_2O abundances in the troposphere compared to 3D studies, hence, the warming due to H_2O absorption would also be underestimated.

2.3. *Photochemistry module BLACKWOLF*

We use BLACKWOLF (BerLin Atmospheric Chemical Kinetics and photochemistry module With application to exOpLanet Findings) to calculate the atmospheric composition profiles of terrestrial planets. BLACKWOLF is based on previous photochemistry module versions (Pavlov & Kasting 2002; Rauer et al. 2011; Gebauer et al. 2018b) which have been used for

[1] www.hitran.org/cia/ (Karman et al. 2019)

Table 1. Species considered in the photochemical model.

Atoms	Species
O, H	O, $O(^1D)$, O_2, O_3, H, H_2, OH, H_2O, HO_2, H_2O_2
C, H	C, C_2, CH, CH_2^3, CH_2^1, CH_3, CH_4, C_2H, C_2H_2, C_2H_3, C_2H_4, C_2H_5, C_2H_6, C_3H_2, C_3H_3, CH_2CCH_2, CH_3C_2H, C_3H_5, C_3H_6, C_3H_7, C_3H_8, C_4H, C_4H_2, C_5H_4
C, O, H	CO, CO_2, HCO, H_2CO, H_3CO, CH_3OH, HCOO, HCOOH, CH_3O_2, CH_3OOH, C_2HO, C_2H_2O, CH_3CO, C_2H_3O, CH_3CHO, C_2H_5O, C_2H_5CHO
N, O	N, N_2, NO, NO_2, NO_3, N_2O, N_2O_5
N, O ,H, C	NH, NH_2, NH_3, HNO, HNO_2, HNO_3, HO_2NO_2, CN, HCN, CNO, HCNO, CH_3ONO, CH_3ONO_2, CH_3NH_2, C_2H_2N, C_2H_4NH, N_2H_2, N_2H_3, N_2H_4
S, O	S, S_2, S_3, S_4, S_5, S_6, S_7, S_8, SO, SO_2, SO_2^1, SO_2^3, SO_3, S_2O, S_2O_2
S, O, H, C	HS, H_2S, HSO, HSO_2, HSO_3, H_2SO_4, CS, CS_2, HCS, CH_3S, CH_4S, OCS, OCS_2
Cl, O	Cl, Cl_2, ClO, OClO, ClOO, Cl_2O, Cl_2O_2
Cl, O, H, N, S	HCl, CH_2Cl, CH_3Cl, HOCl, NOCl, ClONO, $ClONO_2$, COCl, $COCl_2$, $ClCO_3$, SCl, ClS_2, SCl_2, Cl_2S_2, OSCl, $ClSO_2$

NOTE—Each specie only appears once.

multiple studies in our department (e.g. Grenfell et al. 2013, 2014; Scheucher et al. 2018; Wunderlich et al. 2019).

The chemical reactions network of BLACKWOLF is fully flexible in the sense that chemical species and reactions can be easily added or removed. Further, the network can be adapted depending on e.g. the main composition, temperature or surface pressure of the planetary atmosphere in question. The full network consists of 1127 reactions for 128 species, including 832 bi-molecular reactions, 117 termolecular reactions, 53 thermo-dissociation reactions and 125 photolysis reactions. It was developed to compute N_2, CO_2, H_2 and H_2O-dominated atmospheres of terrestrial planets orbiting a range of host stars. The network does not include all forward and backward reactions to consistently simulate equilibrium chemistry for high pressure and high temperature regimes. Hence, we limit the usage of the photochemical module to pressures below 100 bar and temperatures below 800 K. Details of the kinetic reactions can be found in Section 2.3.1.

We consider photochemical reactions for 81 absorbers using wavelength and temperature dependent cross sections. The wavelength and temperature coverage with the corresponding references of all quantum yields and cross sections are given in Table 2 and Table 3. All wavelength dependent data is binned to 133 bands between 100 and 850 nm. See Section 2.3.2 for more details on the selection, binning and interpolation of cross section and quantum yield data. For the two-stream radiative transfer, based on Toon et al. (1989), we consider 81 absorbers and the same eight Rayleigh scatterers as in the climate module (Shardanand & Rao 1977; Allen 1973).

The model considers upper and lower boundary conditions of each chemical specie. At the upper boundary we prescribe atmospheric escape by setting either a fixed flux $\Phi_{\rm TOA}$ in molecules cm^{-2} s^{-1} or an effusion velocity $\nu_{\rm eff}$ in cm s^{-1}. We calculate the molecular diffusion coefficients for the diffusion-limited escape velocity of H and H_2 in N_2, CO_2 or H_2-dominated atmospheres from the parametrization shown in Hu et al. (2012). This was derived from the gas kinetic theory and the coefficients are obtained by fitting to experimental data from Marrero & Mason (1972) and Banks (1973). Following the upper limit of Luger & Barnes (2015) we assume that the oxygen escape flux is one-half the hydrogen escape flux.

The lower model boundary is given by either a fixed volume mixing ratio, f, or a net input or loss at the surface, which depends on the deposition velocity, $\nu_{\rm dep}$ in cm s^{-1}, and the surface emission, $\Phi_{\rm BOA}$ in molecules cm^{-2} s^{-1}. The volcanic flux, $\Phi_{\rm VOLC}$, is distributed over the lower 10 km of the atmosphere. The boundary conditions used for the simulation of the TRAPPIST-1 planetary atmospheres are given in Section 3.3. Tropospheric lightning emissions of nitrogen oxides, NO_x (NO, NO_2), are also included based on the Earth lightning model of Chameides et al. (1977).

To account for the wet deposition of soluble species we use the parametrization of Giorgi & Chameides (1985). This parametrization takes as input effective Henry's law constants, H', of all soluble species. We use the values of H' published in Giorgi & Chameides (1985) as well as the classical Henry's law constants, H, from Sander (2015) and consider available parametrizations of the temperature dependence for the solubility.

In a 1D photochemical model the vertical transport can be approximated by eddy diffusion. In previous model versions the eddy diffusion was fixed to a given profile by Massie & Hunten (1981), which approximates Earth's vertical mixing. BLACKWOLF uses a parametrization of the eddy diffusion coefficient, similar to Gao et al. (2015), which is based on the equations shown in Gierasch & Conrath (1985). We introduce the parametrization and compare eddy diffusion profiles for Earth, Venus and Mars in Section 2.3.3.

Table 2. Reaction rates of bi-molecular reactions (R) in cm^3 s^{-1}, termolecular reactions (M) in cm^6 s^{-1}, thermo-dissociation reactions (T) in s^{-1}, and quantum yields of photolysis reactions (P) used in the photochemical module.

No.	Reaction	Reaction rate or quantum yield	Temperature	Reference
R1	$C + H_2S \rightarrow CH + HS$	$2.1 \cdot 10^{-10}$	298	NIST
R2	$C + O_2 \rightarrow CO + O$	$5.1 \cdot 10^{-11} \cdot (T/298.0)^{-0.3}$	15 - 295	NIST
R3	$C + OCS \rightarrow CO + CS$	$1.01 \cdot 10^{-10}$	298	NIST
M1	$C + H_2 + M \rightarrow CH_2^3 + M$	$k_0 = 7.0 \cdot 10^{-32}$	300	Moses et al. (2011)
		$k_\infty = 2.06 \cdot 10^{-11} \cdot e^{-57.0/T}$		
M2	$CH_3 + CH_3 + M \rightarrow C_2H_6 + M$	$k_0 = 1.68 \cdot 10^{-24} \cdot (T/298.0)^{-7.0} \cdot e^{-1390.0/T}$	300 - 2000	Sander et al. (2011)
		$k_\infty = 6.488 \cdot 10^{-11} \cdot (T/298.0)^{-0.5} \cdot e^{-25.0/T}$		
M3	$CH_3 + O_2 + M \rightarrow CH_3O_2 + M$	$k_0 = 4.0 \cdot 10^{-31} \cdot (T/298.0)^{-3.6}$	200 - 300	NIST
		$k_\infty = 1.2 \cdot 10^{-12} \cdot (T/298.0)^{1.1}$		
T1	$O_3 + M \rightarrow O_2 + O + M$	$7.16 \cdot 10^{-10} \cdot e^{-11200.0/T} \cdot N$	300 - 3000	NIST
T2	$HO_2 + M \rightarrow O_2 + H + M$	$2.41 \cdot 10^{-8} \cdot (T/298.0)^{-1.18} \cdot e^{-24415.0/T} \cdot N$	200 - 2000	NIST
T3	$H_2O_2 + M \rightarrow OH + OH + M$	$2.01 \cdot 10^{-7} \cdot e^{-22852.0/T} \cdot N$	700 - 1500	NIST
P1	$H_2O + h\nu \rightarrow H + OH$	0.89 (100 - 144 nm)	298	Burkholder et al. (2015)
		1 (145 - 198 nm)	298	Burkholder et al. (2015)
P2	$H_2O + h\nu \rightarrow H_2 + O(^1D)$	0.11 (100 - 144 nm)	298	Burkholder et al. (2015)
P3	$HO_2 + h\nu \rightarrow OH + O$	1 (185 - 260 nm)	298	Burkholder et al. (2015)

NOTE—The unit of the temperature, T, is K and the unit of the number density, N, is cm^{-3}. References with * are wavelength and temperature dependent parametrizations of the quantum yields.
(This table is available in its entirety in a machine-readable form in the online journal. A portion is shown here for guidance regarding its form and content.)

Table 3. Cross sections used in the photochemical module. The unit of the wavelengths range is nm and the unit of the temperature range is K.

Specie	Wavelength	Temperature	Reference
O_2	100 - 113	298	Brion et al. (1979)
	115 - 179	298	Lu et al. (2010)
	130 - 175	90 - 298	Yoshino et al. (2005)
	175 - 205	130 - 500	Minschwaner et al. (1992)*
	205 - 245	90 - 298	Burkholder et al. (2015)
	245 - 294	298	Fally et al. (2000)
O_3	110 - 186	298	Mason et al. (1996)
	186 - 213	218 - 298	Burkholder et al. (2015)
	213 - 850	193 - 293	Serdyuchenko et al. (2014)
H_2O	100 - 121	298	Chan et al. (1993)
	121 - 198	298	Burkholder et al. (2015)

NOTE—References with * are wavelength and temperature dependent parametrizations of the cross sections.
(This table is available in its entirety in a machine-readable form in the online journal. A portion is shown here for guidance regarding its form and content.)

2.3.1. *Chemical kinetics*

The chemical network used in previous studies such as Grenfell et al. (2007); Rauer et al. (2011); Grenfell et al. (2013); Wunderlich et al. (2019) is based on Kasting et al. (1985), Pavlov & Kasting (2002) and Segura et al. (2003) and is able to reproduce the Earth's atmosphere with an N_2-O_2-dominated composition. This paper introduces an updated and enhanced network also suitable for CO_2 and H_2-dominated atmospheres. All species included are listed in Table 1 and all reactions can be found in the Table 2. Photochemical reactions are discussed in detail in Section 2.3.2. The chemical network setup is designed to be fully flexible, meaning that subsets of species or reactions can be chosen.

A large number of chemical reactions are taken from the network presented in Hu et al. (2012). Since we focus on the atmosphere of terrestrial planets in the habitable zone around their host stars, we do not include reactions which are only valid at temperatures above 800 K. From the network of Hu et al. (2012) we do not include reactions with hydrocarbon molecules that have more than two carbon atoms. For higher hydrocarbon chemistry we include the reactions up to C_5 shown in Arney et al. (2016). This network has been used and validated in multiple studies focusing on the influence of hydrocarbon haze production on atmospheric composition and climate for a range of different atmospheric conditions (e.g. Arney et al. 2016, 2017, 2018).

Furthermore we update the chlorine chemistry for Earth-like atmospheres with the reaction coefficients from Burkholder et al. (2015) and add new reac-

tions, taken from the online database of the National Institute of Standards and Technology (NIST[2], Mallard et al. 1994). In particular we include reactions which are important for the destruction and build-up of chloromethane (CH_3Cl) for Earth-like atmospheres. Further, we include chlorine and sulphur chemical reactions known to be relevant in CO_2-dominated atmospheres such as Mars and Venus from Zhang et al. (2012). Following e.g. Zahnle et al. (2008) we multiply all termolecular reaction rates by a bathgas factor of 2.5 when CO_2 is the main constituent of the atmosphere and is therefore acting as third body in the termolecular reactions.

If multiple references are found for the same reaction we compare the reaction rates assuming a temperature of 288 K and decide case by case which reaction rate is considered. If the rates do not differ by more than a factor of three, we use the reference which considers a temperature dependence. If non or multiple rates include a temperature dependence we use the reaction rate from the most recent reference. For reaction rates which differ significantly from each other we choose the rate which is in agreement with the rates listed in the NIST database.

To validate that BLACKWOLF is able to simulate the photochemistry of CO_2-dominated atmospheres we model the atmospheres of modern Mars and modern Venus above the cloudtop and compare the results with observations (see Section 2.4).

2.3.2. *Cross sections and quantum yields*

The cross section data are taken from the MPI Mainz Spectral Atlas (Keller-Rudek et al. 2013), the JPL Publication No. 15-10 (Burkholder et al. 2015), Mills (1998) and Zahnle et al. (2008). In the case that there are multiple cross section data available with the same wavelength and temperature coverage, we follow the recommendations of the JPL Chemical Kinetics and Photochemical Data Publication No. 15-10 (Burkholder et al. 2015). If no recommendation was given, we decided case by case which data to use, depending on the consistency of the data with other publications, the year of publication, temperature coverage and wavelength resolution. The quantum yields of the photochemical reactions are taken from Burkholder et al. (2015); Hu et al. (2012); Mills (1998) and the MPI Mainz Spectral Atlas (Keller-Rudek et al. 2013). The wavelength and temperature range with the corresponding references of all quantum yields and cross sections are given in Table 2 and Table 3.

[2] http://kinetics.nist.gov

For cases with a wavelength gap between two datasets we set the cross sections to zero within the gap. We also assume the cross sections to be zero for wavelengths longer or shorter than covered by the available datasets. Quantum yields are interpolated between different datasets. Further, the quantum yields are extrapolated to 100 nm, the lower wavelength limit of the model, and up to the wavelength which corresponds to the bond energy of the reaction stated in Burkholder et al. (2015). Temperature dependent cross sections and quantum yields are interpolated linearly to the temperature of the atmospheric level.

2.3.3. *Eddy diffusion*

The eddy diffusion coefficient, K, in cm^2 s^{-1} as a function of altitude is assumed analogous to that for heat as derived for free convection by Gierasch & Conrath (1985):

$$K = \frac{H}{3}\left(\frac{L}{H}\right)^{4/3}\left(\frac{R\sigma T^4}{\mu\rho C_\mathrm{p}}\right)^{1/3}, \tag{1}$$

where H is the scale height, R is the universal gas constant, σ is the Stefan-Boltzmann constant, μ is the atmospheric molecular weight, ρ is the atmospheric density, C_p is the atmospheric heat capacity, and L is the mixing length.

Equation (1) was also used by e.g. Ackerman & Marley (2001) and Gao et al. (2015) to estimate K. To fit the K profile of Earth, Mars and Venus we adapt the formula for L, which was introduced by Ackerman & Marley (2001):

$$L = \begin{cases} H \cdot \max(0.1, \Gamma/\Gamma_\mathrm{ad}) & z < z_\mathrm{ct} \\ \frac{H_\mathrm{ct}}{4}\left(\frac{20}{p_0} + \left(\frac{1}{p}\right)^{1/4}\right) & z \geq z_\mathrm{ct} \end{cases}, \tag{2}$$

where Γ is the atmospheric lapse rate, Γ_{ad} is the adiabatic lapse rate, p is the atmospheric pressure, p_0 is the surface pressure, z_ct is the height of the cold trap and H_ct is the scale height at z_ct.

For a planet with an ocean, such as Earth, z_ct is the atmospheric layer where water condenses out, i.e. at the lowest layer where $\frac{p_\mathrm{sat}}{p}$ starts to increase with height. p_sat is the saturation pressure of water. For a planet without an ocean, such as Mars and Venus, the eddy diffusion can be well described by breaking gravity waves alone (see e.g. Izakov 2001) and z_ct is set to 0 m.

The left panel of Figure 1 shows the calculated K profile for Earth compared to the K profile derived from trace gases by Massie & Hunten (1981). The gray shaded region represents a range of observational fits from multiple models (Wofsy et al. 1972; Hunten 1975; Allen et al. 1981). The parametrized values match

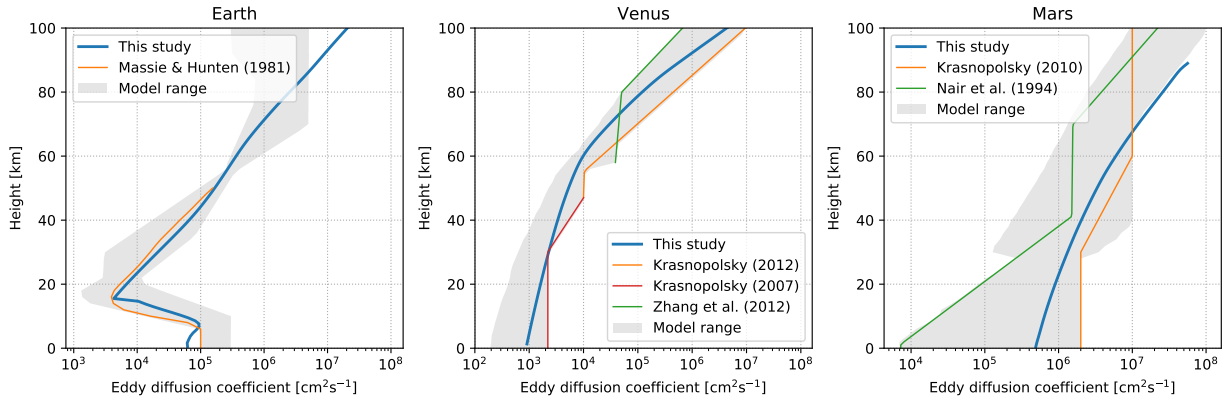

Figure 1. Profiles of eddy diffusion coefficients, K in $\mathrm{cm^2 s^{-1}}$ for modern Earth (left panel), Venus (middle panel) and Mars (right panel) calculated with Eq. (1) shown in blue. The K profile of Earth derived from trace gases by Massie & Hunten (1981) is shown in orange. Assumed profiles for Mars in orange from Krasnopolsky (2010a) and in green from Nair et al. (1994). Assumed profiles for Venus are shown in orange from Krasnopolsky (2012), in red from Krasnopolsky (2007) and in green from Zhang et al. (2012). Gray shading indicates range of K for multiple model studies (see text for details).

well the results shown in Massie & Hunten (1981) and lie within the model range except close to the surface, where surface properties can influence transport and towards the upper mesosphere, where e.g. gravity wave breaking can influence mixing and energy budgets. We do not consider a constant eddy diffusion coefficient profile for Earth in the mesosphere and thermosphere as proposed by e.g. Allen et al. (1981) in order to enable the calculation of K to be as general as possible without further assumptions. For most planets K is found to increase towards high altitudes (see e.g. Zhang & Showman 2018). Note that the model also has the possibility to use a fixed, predefined K profile.

The middle panel of Figure 1 shows reasonable agreement for the calculated K profile of Venus with the assumed profiles from Krasnopolsky (2007), Krasnopolsky (2012) and Zhang et al. (2012). The maximum values of these three studies represent the upper limit of the model range. The lower limit of the model range is taken from Izakov (2001).

The calculated K profile for the Martian atmosphere, compared to the assumed profiles from Krasnopolsky (2010a) and Nair et al. (1994), are shown in the right panel of Figure 1. The lower limit of the model range is from Nair et al. (1994) up to 30 km and from Montmessin et al. (2017) thereabove. The upper limit is from Krasnopolsky (2010a) and Krasnopolsky (2006). Figure 1 shows that the Eq. (1) can represent well the K profiles of Earth, Mars and Venus and hence, is suitable to apply to the scenarios we consider for the TRAPPIST-1 planets.

2.4. *Model validation*

2.4.1. *Earth*

We first validate our model by simulating the modern Earth around the Sun and comparing the results with observations from measurements of the Michelson Interferometer for Passive Atmospheric Sounding (MIPAS; Fischer et al. 2008) and the Atmospheric Chemistry Experiment Fourier Transform Spectrometer (ACE-FTS; Bernath 2017). Details of the MIPAS and ACE-FTS data processing can be found in von Clarmann et al. (2009) and Boone et al. (2005) respectively. The references of the individual datasets for each species can be found on the MIPAS web page [3] and the ACE-FTS web page [4].

We select only the data with high quality, determined as following. For MIPAS data we follow the recommendations that the diagonal element of the averaging kernel needs to be at least 0.03 and the visibility flag must be unity [5]. The ACE-FTS data contains a quality flag indicating physically unrealistic outliers (Sheese et al. 2015). The selected data is averaged for each satellite flyover onto a grid with a resolution of 5° in latitude by 10° in longitude. We repeat this step for each available observation. We take into account 95% of the data and exclude the 5% extremes. The maximum and minimum value for each altitude level represents the measured range shown as gray shading in Figure 2. To calculate the global and annual mean profile of each specie we

[3] www.imk-asf.kit.edu/english/308.php

[4] ace.scisat.ca/publications/

[5] share.lsdf.kit.edu/imk/asf/sat/mesospheo/data/L3/MIPAS_L3_ReadMe.pdf

Table 4. Φ_{BOA} and Φ_{VOLC} of the Earth in molecules cm^{-2} s^{-1}.

Specie	Anthropogenic	Ref.	Biogenic	Ref.	Volcanic	Ref.	Biogenic and Volcanic
O_2	-	-	$1.21{\cdot}10^{12}$	calc.	-	-	$1.21{\cdot}10^{12}$
CH_4	$7.70{\cdot}10^{10}$	(1)	$6.30{\cdot}10^{10}$	(1)	$1.12{\cdot}10^{8}$	(2)	$6.31{\cdot}10^{10}$
CO	$1.16{\cdot}10^{11}$	(3)	$1.07{\cdot}10^{11}$	(3)	$3.74{\cdot}10^{8}$	(2)	$1.07{\cdot}10^{11}$
N_2O	$6.58{\cdot}10^{8}$	(4)	$7.80{\cdot}10^{8}$	(4)	-	-	$7.80{\cdot}10^{8}$
NO	$2.46{\cdot}10^{9}$	(4)	$3.38{\cdot}10^{8}$	(4)	-	-	$3.38{\cdot}10^{8}$
H_2S	$1.97{\cdot}10^{7}$	(5)	$1.84{\cdot}10^{9}$	(5)	$1.89{\cdot}10^{9}$	(2)	$3.73{\cdot}10^{9}$
SO_2	$1.70{\cdot}10^{10}$	(5)	-	-	$1.34{\cdot}10^{10}$	(2)	$1.34{\cdot}10^{10}$
NH_3	$3.57{\cdot}10^{9}$	(6)	$8.15{\cdot}10^{8}$	(6)	-	-	$8.15{\cdot}10^{8}$
OCS	$4.54{\cdot}10^{7}$	(7)	$1.39{\cdot}10^{8}$	(7)	$2.67{\cdot}10^{6}$	(7)	$1.42{\cdot}10^{8}$
HCN	$1.32{\cdot}10^{8}$	(8)	$1.27{\cdot}10^{7}$	(8)	-	-	$1.27{\cdot}10^{7}$
CH_3OH	$2.91{\cdot}10^{9}$	(9)	$3.35{\cdot}10^{10}$	(9)	-	-	$3.35{\cdot}10^{10}$
CS_2	$1.15{\cdot}10^{8}$	(7)	$4.98{\cdot}10^{8}$	(7)	$6.23{\cdot}10^{6}$	(7)	$5.05{\cdot}10^{8}$
CH_3Cl	$7.97{\cdot}10^{7}$	(4)	$1.39{\cdot}10^{8}$	(4)	-	-	$1.39{\cdot}10^{8}$
C_2H_2	$9.48{\cdot}10^{8}$	(8)	-	-	-	-	-
C_2H_6	$7.09{\cdot}10^{8}$	(4)	$8.50{\cdot}10^{8}$	(10)	$5.10{\cdot}10^{6}$	(10)	$8.55{\cdot}10^{8}$
C_3H_8	$5.52{\cdot}10^{8}$	(10)	$9.49{\cdot}10^{8}$	(10)	$2.29{\cdot}10^{6}$	(10)	$9.51{\cdot}10^{8}$
HCl	$1.32{\cdot}10^{9}$	(11)	$5.13{\cdot}10^{9}$	(11)	$4.42{\cdot}10^{8}$	(12)	$5.57{\cdot}10^{9}$
H_2	$7.43{\cdot}10^{10}$	(3)	$1.86{\cdot}10^{10}$	(3)	$3.75{\cdot}10^{9}$	(2)	$2.23{\cdot}10^{10}$

NOTE—The biogenic flux of O_2 corresponds to the value necessary to reproduce a volume mixing ratio of O_2 of 0.21 on modern Earth, assuming a deposition velocity of $1{\cdot}10^{-8}$cm/s. (1) Lelieveld et al. (1998); (2) Catling & Kasting (2017); (3) Hauglustaine et al. (1994); (4) Seinfeld & Pandis (2016); (5) Berresheim et al. (1995); (6) Bouwman et al. (1997); (7) Khalil & Rasmussen (1984); (8) Duflot et al. (2015); (9) Tie et al. (2003); (10) Etiope & Ciccioli (2009); (11) Legrand et al. (2002); (12) Pyle & Mather (2009)

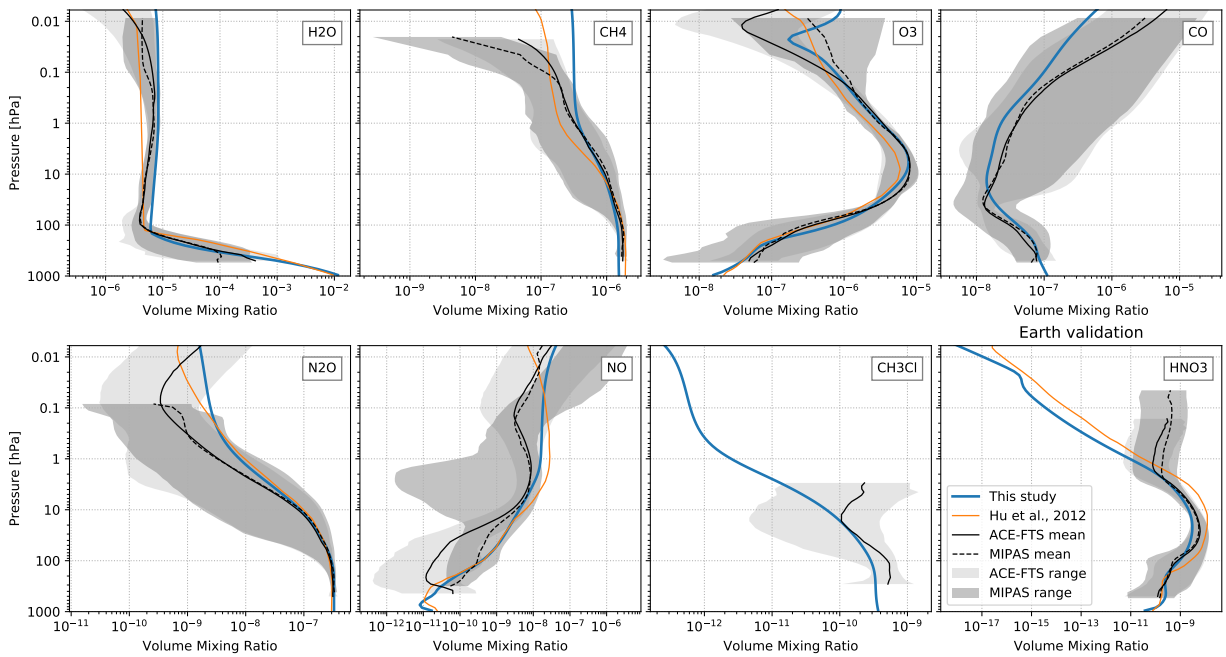

Figure 2. Earth composition profiles for selected species predicted with our photochemistry model shown in blue, compared to the results from Hu et al. (2012) in orange and to MIPAS and ACE-FTS measurements in black. Dark gray shaded regions indicate MIPAS measurement ranges whereas light gray shaded regions indicate ACE-FTS measurement ranges (see text for details).

Table 5. ν_{dep} as measured for the Earth in cm s^{-1}.

Specie	ν_{dep} (cm s^{-1})	Reference
O_2	$1{\cdot}10^{-8}$	Arney et al. (2016)
O_3	0.4	Hauglustaine et al. (1994)
H_2O_2	1	Hauglustaine et al. (1994)
CO	0.03	Hauglustaine et al. (1994)
CH_4	$1.55{\cdot}10^{-4}$	Watson (1992)
NO	0.016	Hauglustaine et al. (1994)
NO_2	0.1	Hauglustaine et al. (1994)
NO_3	0.1	Hauglustaine et al. (1994)
N_2O_5	4	Hauglustaine et al. (1994)
HNO_3	4	Hauglustaine et al. (1994)
HO_2NO_2	0.4	Hauglustaine et al. (1994)
SO_2	1	Sehmel (1980)
NH_3	1.7075	Phillips et al. (2004)
OCS	0.01	Seinfeld & Pandis (2016)
CH_3OOH	0.25	Hauglustaine et al. (1994)
HCl	0.8	Kritz & Rancher (1980)
HCN	0.044	Duflot et al. (2015)
CH_3OH	1.26	Tie et al. (2003)

NOTE—For all other species we use ν_{dep} of 0.02 cm s^{-1}, following Hu et al. (2012) and Zahnle et al. (2008).

calculate a monthly mean and from that an annual mean at each grid point. This ensures that each season of the year is equally represented. Finally we average over the grid with a zonal and weighted meridional mean.

Different to our previous studies we do not tune the surface fluxes to reproduce the observed surface abundances of CO, NO_2, CH_4 and CH_3Cl (e.g. Grenfell et al. 2013, 2014; Wunderlich et al. 2019). Instead we use the sum of observed anthropogenic, biogenic and volcanic surface fluxes (see Table 4) and observed ν_{dep} (see Table 5). Also included are modern-day tropospheric lightning emissions of NO_x. We apply an upper boundary condition for H and H_2 with the parametrization from Hu et al. (2012). To simulate modern Earth we use the solar spectrum from Gueymard (2004). The temperature profile simulated with the model is shown in the companion paper (Scheucher et al. accepted). To achieve a mean surface temperatures of 288.15 K in our cloud-free model we use a surface albedo of 0.255.

Figure 2 shows that the photochemistry of the Earth can be reproduced well with the new chemical network. We also compare well to the results shown by Hu et al. (2012). Tropospheric abundances of all shown species lie within the measurement range. In the upper stratosphere and mesosphere the abundances of HNO_3 are underestimated in both models compared to measurements. This discrepancy could be due to missing NO_x-related processes, such as energetic particle precipitation, producing NO_x in the upper mesosphere and subsequent dynamical transport into the stratosphere (see e.g. Krivolutsky 2001; Siskind et al. 2000; López-Puertas et al. 2005; Clilverd et al. 2009; Funke et al. 2005, 2010, 2014, 2016).

2.4.2. *Mars*

As a second validation case we simulate the atmosphere of modern Mars. We use the atmospheric temperature profile from Haberle et al. (2017), representing a scenario with weak dust loading. The data is based on diurnal averages of Mars Climate Sounder (MCS) observations (Kleinböhl et al. 2009). The radiative-convective climate module is not used here to calculate the temperature profile since we want to focus on the validation of the photochemistry model. The climate validation for Mars is presented in Scheucher et al. (accepted). The mean surface pressure of the reference atmosphere is 5.62 hPa (Haberle et al. 2017). We use a bond albedo of 0.25 (Williams 2010). The eddy diffusion coefficients are directly calculated in the model (see Section 2.3.3).

In Table 6 we show the boundary conditions used to model the Martian atmosphere. N_2 serves as a fill gas and is 2.82% over the entire atmosphere, which is similar to the measurements of Owen et al. (1977) which suggested a volume mixing ratio of 2.7%.

Figure 3 shows the profile of selected atmospheric species compared to the model results of Krasnopolsky (2010a) and the following measurements. For H_2O we take into account Mars Express PFS (Planetary Fourier Spectrometer) nadir measurements up to 30 km from Montmessin & Ferron (2019) and SPICAM (Spectroscopy for the Investigation of the Characteristics of the Atmosphere of Mars) measurements above 20 km from Fedorova et al. (2009). O_3 ranges are taken from nighttime and sunrise/sunset measurements (Montmessin & Lefèvre 2013; Lebonnois et al. 2006). CO observational ranges are taken from retrieval uncertainties around 800 ppm from PFS/Mars Express infrared nadir observations (Bouche et al. 2019). The H_2 range at 80 km is given in Krasnopolsky & Feldman (2001) and O_2 range at the surface is taken from Trainer et al. (2019). We compute the observational ranges by finding the lowest and highest value in a 2 km grid from measured profiles or observations of the mixing ratio at a given altitude. Note that surface values are located at 1 km for visibility purposes.

The Martian atmosphere simulated with the photochemistry model compares well with the results from Krasnopolsky (2010a) and Nair et al. (1994). The model simulates H_2O abundances close to the lower minimum

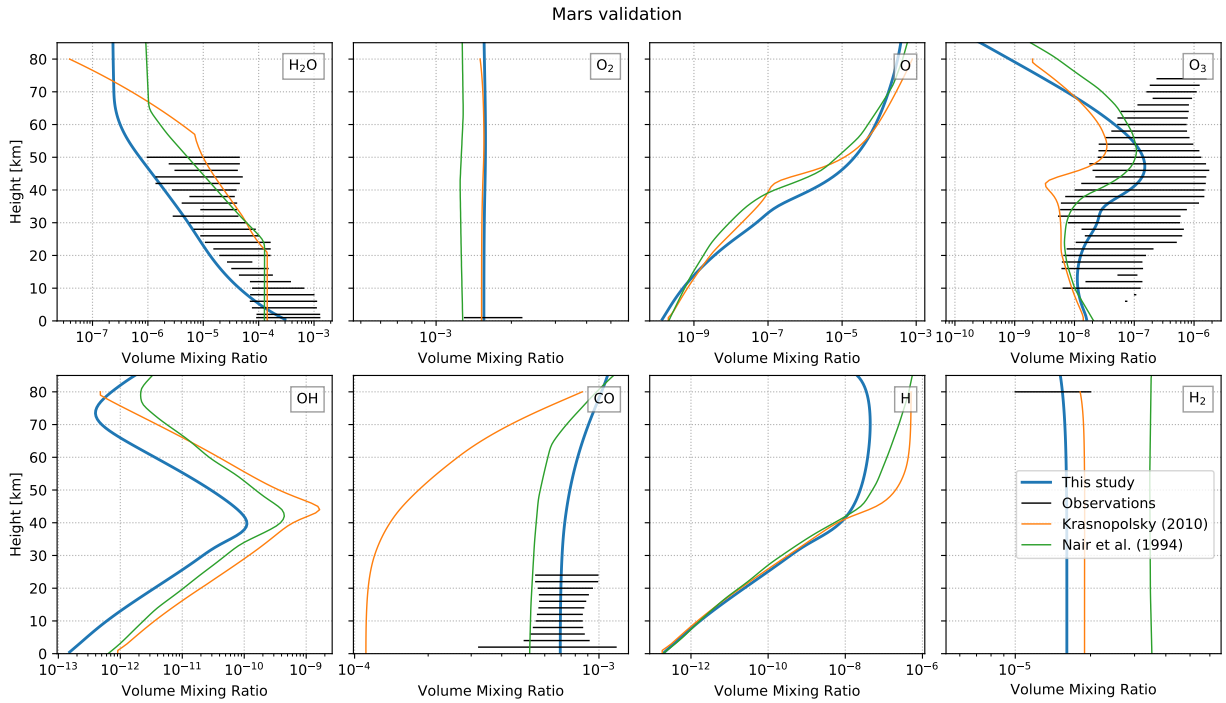

Figure 3. Mars composition profiles for selected species predicted with our photochemistry model shown in blue, compared to the results from Krasnopolsky (2010a) in orange, Nair et al. (1994) in green and a range of multiple observations in black (see text for details).

of measured concentrations. When using an eddy diffusion flux increased by a factor of ten, more water is transported upwards and the modelled H_2O abundances fit to the measurements (not shown). Since we model an aerosol free atmosphere the low H_2O content is consistent with observations of Vandaele et al. (2019) showing increased atmospheric H_2O during dust storms. Note that Krasnopolsky (2010a) and Nair et al. (1994) used a predefined H_2O profile while we calculate the H_2O profile consistently in the photochemical model. The underestimation of the O_3 content above 60 km may be related to diurnal changes in the solar zenith angle, not included in the model. We obtain a surface O_2 concentration of 1552 ppm which is consistent with the global mean of 1560±54 ppm inferred by Krasnopolsky (2017) and also in the range of the seasonal variation of O_2 (1300 - 2200 ppm, Trainer et al. 2019).

In summary we show that our photochemistry model gives consistent results compared to previous photochemistry models and observations of the Martian atmosphere. Different from many previous models, we also simulate consistently the chemistry of chlorine, sulphur and methane. The emission fluxes required to reproduce observations of CH_4, HCl and SO_2 are shown in Table 6. The Martian CH_4 chemistry will be discussed in detail in a follow up paper by Grenfell et al. (in prep).

2.4.3. *Venus*

Predicting the atmospheric composition of Venus is challenging since details of the sulphur chemistry are not understood completely (e.g. Mills & Allen 2007; Zhang et al. 2012; Vandaele et al. 2017). The atmospheric chemistry of Venus below and above the cloud deck is usually modeled separately. We validate our model by calculating the atmosphere of Venus only in the photochemical regime above the cloud top at ∼58 km, where direct observations of chemical species are available. The temperature profile is taken from the Venus International Reference Atmosphere VIRA-1 (Seiff et al. 1985).

The boundary conditions are presented in Table 7. Following Zhang et al. (2012) and Krasnopolsky (2012) we use fixed volume mixing ratios at BoA for key species to fit the observed values and we assume a downward flux of all other species depending on K and H (see also Section 2.3.3). Figure 4 shows the profiles of the species with existing observations and profiles taken from Zhang et al. (2012) and Krasnopolsky (2012).

The range of observational values is derived by combining multiple studies. The H_2O range is generated by combining measurements from Bertaux et al. (2007) and measurements shown in Figure 3 of Krasnopolsky (2012). CO measurements are taken from Svedhem et al. (2007) and Figure 2 of Krasnopolsky (2012). HCl measurements are taken from Sandor & Clancy (2012) and

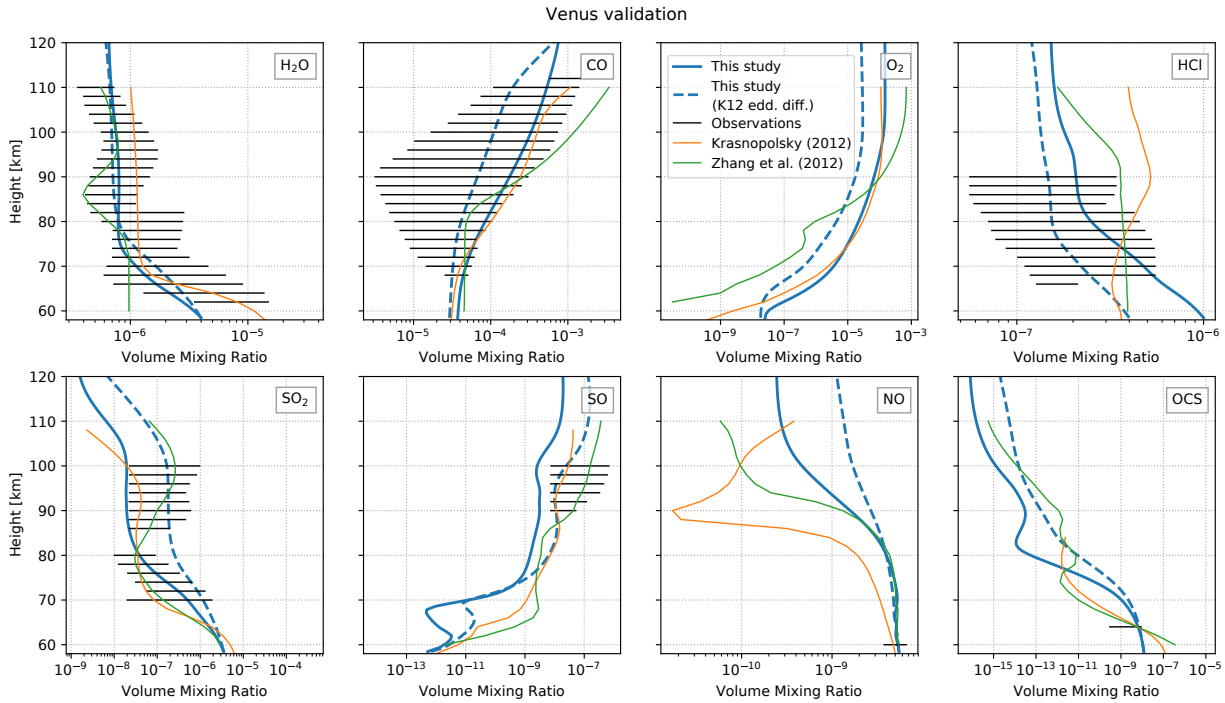

Figure 4. Venus composition profiles for selected species predicted with our photochemistry model with calculated K (solid blue line) and with K taken from Krasnopolsky (2012) with breakpoint h_e at 65 km (K12 edd. diff., dashed blue line), compared to the results from Krasnopolsky (2012), Zhang et al. (2012) and a range of observations inferred from multiple studies (see text for details).

Bertaux et al. (2007). For the observational range of SO_2 and SO we use Venus Express solar occultations in the infrared range and SPICAV (Spectroscopy for Investigation of Characteristics of the Atmosphere of Venus) occultations from Belyaev et al. (2012) and submillimeter measurements from Sandor et al. (2010). The OCS observation is taken from Krasnopolsky (2010b) and NO measurements from Krasnopolsky (2006). As for the Mars validation we compute the observational ranges by finding the lowest and highest value in a 2 km grid.

We find that our model is able to reproduce the Venus atmosphere above 58 km and leads to broadly comparable results as for other photochemical models. Our model reproduces the measurements best with a H_2O mixing ratio of $4.0{\cdot}10^{-6}$, which is in between the values shown in Krasnopolsky (2012) and Zhang et al. (2012). The HCl profile of our model is consistent with the decrease between 70 and 100 km found by observations (Sandor & Clancy 2012) and was not reproduced by the models of Krasnopolsky (2012) and Zhang et al. (2012). On using our calculated eddy diffusion coefficients we underestimate the abundances of SO_2 and SO between 90 and 100 km. Using larger eddy diffusion coefficients from Krasnopolsky (2012) we then lie in the observational range of SO_2 and SO between 90 and 100 km but slightly overestimate the SO_2 abundances around 80 km. This degeneracy may be caused by the missing consideration of sulphur hazes in the upper atmosphere (see e.g. Gao et al. 2014).

In summary we find that we can predict the upper atmosphere of Venus similarly well as other models, even without consideration of the effect of hazes above the cloud layer.

2.5. *Transmission spectra*

The climate-photochemistry model is used to simulate atmospheric temperature and composition profiles of potential atmospheres of TRAPPIST-1 e and TRAPPIST-1 f. With the resulting profiles we produce transmission spectra of the planetary atmospheres using the "Generic Atmospheric Radiation Line-by-line Infrared Code" (GARLIC; Schreier et al. 2014, 2018). GARLIC has been used in recent exoplanet studies such as Scheucher et al. (2018); Katyal et al. (2019); Wunderlich et al. (2019).

We simulate transmission spectra including 28 atmospheric species[6] between 0.4 μm and 12 μm. Line parameters are taken from the HITRAN 2016 database

[6] OH, HO_2, H_2O_2, H_2CO, H_2O, H_2, O_3, CH_4, CO, N_2O, NO, NO_2, HNO_3, ClO, CH_3Cl, HOCl, HCl, $ClONO_2$, H_2S, SO_2, O_2, CO_2, N_2, C_2H_2, C_2H_4, C_2H_6, NH_3, HCN

Table 6. Boundary conditions of modern Mars.

Specie	Lower	Ref.	Upper	Ref.
CO_2	$f = 0.9532$	(1)	$\Phi_{TOA} = 0$	-
H_2O	$f = 3{\cdot}10^{-4}$	(1)	$\Phi_{TOA} = 0$	-
CH_4	$\Phi_{BOA} = 7.5{\cdot}10^{3}$	(2)	$\Phi_{TOA} = 0$	-
SO_2	$\Phi_{BOA} = 1.5{\cdot}10^{6}$	(3)	$\Phi_{TOA} = 0$	-
HCl	$\Phi_{BOA} = 2.4{\cdot}10^{4}$	(4)	$\Phi_{TOA} = 0$	-
H_2	$\Phi_{BOA} = 0$	-	$\nu_{eff} = 3.39$	(5)
H	$\Phi_{BOA} = 0$	-	$\nu_{eff} = 3080$	(6)
O	$\Phi_{BOA} = 0$	-	$\Phi_{TOA} = 1{\cdot}10^{7}$	(7)
O_2	$\nu_{dep} = 1{\cdot}10^{-8}$	(8)	$\Phi_{TOA} = 0$	-
CO	$\nu_{dep} = 1{\cdot}10^{-8}$	(9)	$\Phi_{TOA} = 0$	-
other	$\nu_{dep} = 2{\cdot}10^{-2}$	(7)	$\Phi_{TOA} = 0$	-

NOTE—See Section 2.3 for description of how the boundaries are included in the model. Φ_{BOA} and Φ_{TOA} are in molecules cm^{-2} s^{-1}, ν_{dep} and ν_{eff} are in cm s^{-1}. Following Zahnle et al. (2008), for all species not listed here we assume a ν_{dep} of 0.02 cm s^{-1}. (1) Owen et al. (1977), (2) Φ_{BOA} necessary to fit the mean surface value of $f_{CH_4} = 4{\cdot}10^{-10}$ (Webster et al. 2018), (3) Φ_{BOA} necessary to fit the upper limit of $f_{SO_2} = 3{\cdot}10^{-10}$ (Encrenaz et al. 2011), (4) Φ_{BOA} necessary to fit the upper limit of $f_{HCl} = 2{\cdot}10^{-10}$ (Hartogh et al. 2010), (5) ν_{eff} necessary to fit $f_{H_2} = 1.5{\cdot}10^{-5}$ at TOA (Krasnopolsky & Feldman 2001); Nair et al. (1994) used $\nu_{eff} = 33.9$ cm s^{-1}, (6) Nair et al. (1994), (7) Zahnle et al. (2008), (8) Arney et al. (2016), (9) Kharecha et al. (2005). We use a constant volume mixing ratio of argon profile of 1.6% (Owen et al. 1977). N_2 serves as a fillgas.

Table 7. Boundary conditions of modern Venus.

Specie	Lower	Ref.
CO_2	$f = 0.965$	Zhang et al. (2012)
CO	$\nu_m = 0.1K/H$	Krasnopolsky (2012)
H2O	$f = 4.0{\cdot}10^{-6}$	tuned
OCS	$f = 1.2{\cdot}10^{-8}$	tuned
NO	$f = 5.5{\cdot}10^{-9}$	Zhang et al. (2012)
HCl	$f = 1{\cdot}10^{-6}$	tuned (calc. edd. diff.)
HCl	$f = 4{\cdot}10^{-7}$	Zhang et al. (2012) (K12 edd. diff.)
SO2	$f = 3.5{\cdot}10^{-6}$	Zhang et al. (2012)
other	$\nu_m = K/H$	Zhang et al. (2012)

NOTE—For all species not listed here we assume a maximum deposition velocity $\nu_m = K/H$, using K and H at 58 km to take into account that our BoA is not the surface (see Zhang et al. 2012; Krasnopolsky 2012). $f_{HCl} = 1{\cdot}10^{-6}$ for the run with a calculated K and $f_{HCl} = 4{\cdot}10^{-7}$ for the run with K taken from Krasnopolsky (2012). N_2 serves as fillgas.

(Gordon et al. 2017) and the Clough-Kneizys-Davies (CKD) continuum model (Clough et al. 1989). Additionally Rayleigh extinction is considered (Murphy 1977; Clough et al. 1989; Sneep & Ubachs 2005; Marcq et al. 2011). In the visible we use the cross sections at room temperature (298 K) for O_3, NO_2, NO_3 and HOCl listed in Table 3.

For the 1D climate-photochemistry simulations we do not consider cloud formation. Hence, all the transmission spectra we calculate in this study show cloud-free conditions. However, an Earth-like extinction from uniformly distributed aerosols in the atmosphere can be considered in GARLIC. The aerosol optical depth, τ_A, at wavelength λ (μm) is expressed following Ångström (1929, 1930):

$$\tau_A = \beta \cdot \lambda^{-\alpha}, \tag{3}$$

assuming that the aerosol size distribution follows the Junge distribution (Junge 1952, 1955). For the exponent, α, we use 1.3, representing the average measured value on Earth (see e.g. Ångström 1930, 1961). The Ångström turbidity coefficient, β, is expressed using the cross section data for the Earth's atmosphere taken from Allen (1976):

$$\beta = 1.4 \cdot 10^{-27} \cdot N_c, \tag{4}$$

where N_c is the column density in molecules cm^{-2} (see also Toon & Pollack 1976; Kaltenegger & Traub 2009; Yan et al. 2015). According to Allen (1976) the Eq. (4) corresponds to clear atmospheric conditions with weak scattering by haze or dust.

The transmission spectra from GARLIC are expressed as effective heights:

$$h_e(\lambda) = \int_0^{ToA} \Big(1 - \mathcal{T}(\lambda, z)\Big)\, dz, \tag{5}$$

where $\mathcal{T}$ is the transmission along the limb with the tangent altitude, z. h_e is the integration over all $\mathcal{T}$ from the surface to the top of atmosphere (ToA) at each wavelength, λ. The measured transit depth, t_{depth}, of a planet with an atmosphere is the sum of the planet radius, R_p, and h_e with respect to the stellar radius, R_s. The atmospheric transit depth, t_{atm}, only contains the contribution of the atmosphere to the total transit depth:

$$t_{atm}(\lambda) = \frac{(R_p + h_e(\lambda))^2}{R_s^2} - \frac{R_p^2}{R_s^2}. \tag{6}$$

In order to detect a spectral feature we make use of the wavelength dependence of t_{atm}. To extract the measurable atmospheric signal, S_{atm}, we subtract the minimum

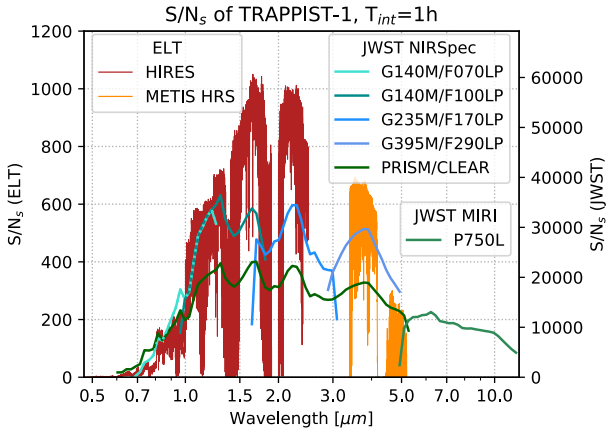

Figure 5. Stellar S/N of TRAPPIST-1 for 1 h integration time and binned to a resolving power of R=100,000 for ELT (left y-axis) and a R=30 for JWST (right y-axis). The conversion factor from the right to the left y-axis is $\sqrt{\frac{100{,}000}{30}}$, corresponding to a white noise binning of the S/N$_s$. The stellar S/N of JWST is the combination of all NIRSpec filter and disperser and MIRI LRS, calculated with the method presented in Wunderlich et al. (2019). We do not consider a partial saturation strategy as suggested by Batalha et al. (2018). The stellar S/N of ELT is calculated with the ESO ETC Version 6.4.0 (Liske 2008).

atmospheric transit depth, $t_{\rm min}$, in the considered wavelength range (baseline) from the $t_{\rm atm}$ at each wavelength point:

$$t_{\rm min} = \min\left(t_{\rm atm}(\lambda)\right), \tag{7}$$

$$S_{\rm atm}(\lambda) = t_{\rm atm}(\lambda) - t_{\rm min}. \tag{8}$$

The wavelength dependent $S_{\rm atm}$, expressed as parts per million (ppm), is used to calculate the signal-to-noise ratio (S/N) of molecular features. Taking into account the $h_{\rm e}(\lambda)$ instead would overestimate the S/N of the spectral features, because that measure would include the continuum extinction.

2.6. *Signal-to-noise ratio (S/N)*

We determine which atmospheric spectral features of the simulated atmospheres of TRAPPIST-1 e and TRAPPIST-1 f could be detectable with ELT and JWST. Lustig-Yaeger et al. (2019) showed that the S/N for emission spectroscopy of TRAPPIST-1 e and TRAPPIST-1 f is too low to detect spectral features (see also Batalha et al. 2018). Hence, we limit our analysis to transmission spectroscopy.

To calculate the S/N of planetary atmospheric feature, S/N$_{\rm atm}$, of a single transit, we first calculate the S/N of the star, S/N$_{\rm s}$, integrated over one transit and then multiply this value with $S_{\rm atm}$:

$$\mathrm{S/N}_{\rm atm} = \frac{S_{\rm atm}}{\sqrt{2}} \cdot \mathrm{S/N}_{\rm s}. \tag{9}$$

The factor $\frac{1}{\sqrt{2}}$ accounts for the fact that the star is observed during in transit and out of transit. We calculate the number of transits, $n_{\rm tr}$, necessary to reach an S/N of 5, assuming that all transits improve S/N$_{\rm s}$ perfectly. The S/N$_{\rm s}$ for JWST NIRSpec and MIRI is determined by the method and instrument specifications presented in Wunderlich et al. (2019) (see Table 8 for the wavelength coverage and resolving power, $R = \frac{\lambda}{\Delta\lambda}$).

The S/N$_{\rm s}$ of the ELT High Resolution Spectrograph (HIRES; Marconi et al. 2016) is calculated with the ESO Exposure Time Calculator[7] (ETC) Version 6.4.0 from November 2019 (see updated documentation[8] from Liske 2008). The ETC uses the background sky model[9] for the Cerro Paranal and considers photon and as well as detector noises such as readout noise and dark current. The ETC assumes a spectrograph with a throughput of 25%, independent of the resolving power. For HIRES or METIS HRS this value might overestimate the real value. For METIS HRS the expected throughput ranges between 6% and 21% (Cárdenas Vázquez, personal communication). Hence, we scale down the S/N$_{\rm s}$ for both instruments to an average throughput of 10%.

We assume a telescope with a diameter of 39 m at Paranal in Chile (2,635 m). The planned location of the ELT at Cerro Armazones (3,046 m) is not available in the ETC. The sky conditions are set to a constant airmass of 1.5 and a precipitable water vapour (PWV) of 2.5 (Liske 2008). The ETC does not provide the possibility to choose the individual ELT instrumentations but we consider the wavelength coverage and R for the instruments planned for the ELT (see Table 8). For each wavelength band we change the radius of the diffraction limited core of the point spread function according to the recommendation in the ETC manual. The wavelengths from 2.9 μm to 3.4 μm cannot be calculated by the current version of the ETC.

To simulate an observation of TRAPPIST-1 we scale the stellar spectrum from Wilson et al. (submitted) to the J-band magnitude of 11.35 (Gillon et al. 2016) in order to obtain the input flux distribution.

[7] https://www.eso.org/observing/etc/bin/gen/form?INS.NAME=E-ELT+INS.MODE=swspectr

[8] https://www.eso.org/observing/etc/doc/elt/etc_spec_model.pdf

[9] https://www.eso.org/sci/facilities/eelt/science/drm/tech_data/background/

Table 8. Wavelength coverage and resolving power, R, of the instruments on JWST and ELT used to calculate SNR_s of TRAPPIST-1.

Telescope	Instrument	Wavelength	R	Reference
JWST	NIRSpec PRISM/CLEAR	0.6 - 5.3 μm	∼100	Birkmann et al. (2016)
JWST	NIRSpec G140M/F070LP	0.7 - 1.27 μm	∼1,000	Birkmann et al. (2016)
JWST	NIRSpec G140M/F100LP	0.97 - 1.84 μm	∼1,000	Birkmann et al. (2016)
JWST	NIRSpec G235M/F170LP	1.66 - 3.07 μm	∼1,000	Birkmann et al. (2016)
JWST	NIRSpec G395M/F290LP	2.87 - 5.10 μm	∼1,000	Birkmann et al. (2016)
JWST	MIRI P750L (LRS)	5.0 - 12 μm	∼100	Kendrew et al. (2015)
ELT	HIRES	0.37 - 2.5 μm	100,000	Marconi et al. (2016)
ELT	METIS (HRS)	2.9 - 5.3 μm	100,000	Brandl et al. (2016)

The S/N_s for a one hour integration of TRAPPIST-1 for JWST and ELT is shown in Figure 5. The ground-based facility ELT will have a much larger telescope area compared to the space-borne JWST but its capability of detecting spectral features with low resolution spectroscopy is limited to atmospheric windows with minor telluric contamination. However, high-resolution spectra ($R > 25{,}000$) resolve individual lines improving their detectability. The Doppler-shift of the lines during the transit with respect to the absorption lines of the Earth's atmosphere is measurable for close-in planets (see e.g. Birkby 2018). Previous theoretical and observational studies have shown that a detection of molecules such as O_2, H_2O or CO is feasible via cross-correlation (e.g. Snellen et al. 2013; Birkby et al. 2013; Brogi et al. 2018; Mollière & Snellen 2019; López-Morales et al. 2019; Sánchez-López et al. 2019).

We adopt a simple approach in order to estimate the number of transits which are necessary to detect e.g. O_2, H_2O and CO with the cross-correlation method in our simulated atmospheres. We adapted a formula presented in Snellen et al. (2015) to calculate the signal-to-noise ratio of the planet, considering the wavelength dependency of $S_{\rm atm}$ and S/N_s

$$S/N_{\rm atm} = \frac{\sum_{l=0}^{n_l} S_{\rm atm}(\lambda_l) \cdot S/N_s(\lambda_l)}{n_l} \cdot \sqrt{t_{\rm int}} \cdot \sqrt{n_l}, \quad (10)$$

where n_l is the number of spectral lines and $t_{\rm int}$ is the integration time. $t_{\rm int}$ is calculated by $t_{\rm dur} \cdot n_{\rm tr}$, with the transit duration, $t_{\rm dur}$, and the number of transits, $n_{\rm tr}$. The S/N_s at the wavelength of the line, λ_l, used in Eq. (10), is the S/N_s shifted by one bandwidth to account for the displacement of the spectral line during transit.

Using Eq. (10) we find that a 3σ detection of O_2 on an Earth-twin around an M7 star at a distance of 5 pc might be feasible when co-adding 58 transit observations in the J-band with ELT HIRES, assuming a throughput of 20%. Rodler & López-Morales (2014) suggested that 26 transits are needed to detect O_2 when using the same assumptions.

Section 4.5.6 discusses the detectability of the CO spectral feature in the atmosphere of a hypothetical planets around other low mass stars in the solar neighbourhood. For stars on the Northern sky we calculate the S/N_s for the Thirty Meter Telescope (TMT, Nelson & Sanders 2008). This will have a smaller telescope area than the ELT but will be located at a higher altitude of 4,064 m, compared to 2,635 m at Paranal. Hence, due to the lower PWV and weaker high-altitude turbulence at Mauna Kea the TMT is expected to have a similar performance as the ELT. We compare the S/N_s of ELT with R=4,000 at a Vega magnitude of 16 in the J-band to calculation of the S/N_s with the same specifications using the Infrared Imaging Spectrograph (IRIS) on TMT by Wright et al. (2014) and find that ELT has a 10% lower S/N_s than TMT.

Since the performance of the telecopes during operation is not yet established we simply assume that the TMT provides the same S/N_s as the ELT.

3. STELLAR INPUT AND MODEL SCENARIOS

3.1. *TRAPPIST-1 spectra*

The Spectral Energy Distribution (SED) in the UV has a large impact on the photochemisty of atmospheres of terrestrial planets (see e.g. Selsis et al. 2002; Grenfell et al. 2013, 2014; Tian et al. 2014). In this study we use the semi-empirical model spectrum of TRAPPIST-1 from Wilson et al. (submitted), which we will refer to as W20 SED. The constructed SED uses observational data from XMM-Newton for the X-ray regime and from the Hubble Space Telescope (HST) for the 113 to 570 nm range with a gap between 208-279 nm obtained through the Mega-MUSCLES Treasury survey (Froning et al. 2018). The wavelengths larger than 570 nm are

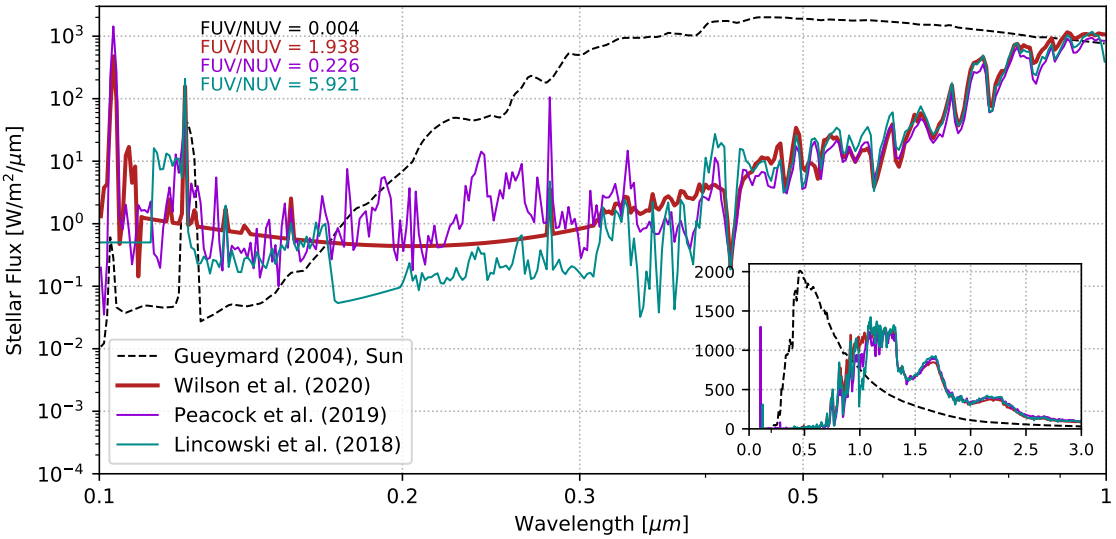

Figure 6. Input stellar spectral energy distribution (SED) of TRAPPIST-1 and the Sun. Red line: TRAPPIST-1 SED with the UV estimated with a semi-empirical model using HST observational data provided by the Mega-MUSCLES survey (Wilson et al. submitted), marked W20 SED. Cyan line: TRAPPIST-1 SED with estimated UV flux by scaling the spectrum of Proxima Centauri (Lincowski et al. 2018), marked L18 SED. Violet line: TRAPPIST-1 SED with calculated UV flux using a semi-empirical non-LTE model Peacock et al. (2019), marked P19 SED. Black line: solar SED taken from Gueymard (2004). For the FUV/NUV ratio the FUV is integrated between 117-175 nm and the NUV is integrated over 175-320 nm (see Tian et al. 2014).

filled by Wilson et al. (submitted) with a PHOENIX photospheric model (Allard 2016; Baraffe et al. 2015).

Figure 6 compares the Mega-MUSCLES TRAPPIST-1 SED with spectra, presented in previous studies. Lincowski et al. (2018) estimated the UV radiation of TRAPPIST-1 by scaling the Proxima Centauri's spectrum to the Lyα measurements of TRAPPIST-1 from Bourrier et al. (2017), in the following referred to as L18 SED. Peacock et al. (2019) present a semi-empirical non-local thermodynamic equilibrium (non-LTE) model spectrum of TRAPPIST-1, based on the stellar atmosphere code PHOENIX (Hauschildt 1993; Hauschildt & Baron 2006; Baron & Hauschildt 2007), here referred to as P19 SED.

We bin all spectra into 128 bands for the climate model and 133 bands for the photochemistry model. The spectra for TRAPPIST-1, as well as the solar spectrum from Gueymard (2004) are shown in Figure 6. All SEDs are scaled to an integrated total energy of 1361 W/m^2 which is equal to the energy the Earth receives from the Sun.

3.2. *System parameters and habitability*

We use the following stellar parameters of TRAPPIST-1: a $T_{\rm eff}$ of 2516 K (Van Grootel et al. 2018), a radius of 0.124 $R_\odot$ (Kane 2018), a mass of 0.089 $M_\odot$ (Van Grootel et al. 2018) and a distance of 12.43 pc (Kane 2018). Table 9 provides the planetary parameters for planet e and f used to model the atmosphere and to calculate the S/N of the produced transmission spectra. We do not focus here on TRAPPIST-1 g since initial studies with our model (not shown) suggested cold, non-habitable conditions, even assuming several tens of bar of surface CO2, although this is a subject for future study (see e.g. Wolf 2017; Turbet et al. 2018; Lincowski et al. 2018).

Most previous studies used the planetary parameters from Gillon et al. (2017) with an irradiation of 0.662 S$_\odot$

Table 9. Planetary parameters used as input for the climate-photochemistry model and to calculate the S/N of spectral features. The planetary radii from Delrez et al. (2018a) are corrected according to Kane (2018). The gravity is calculated using given planetary mass and radius.

Planets	e	f	Reference
Radius ($R_\oplus$)	0.94	1.08	Kane (2018)
Mass ($M_\oplus$)	0.772	0.934	Grimm et al. (2018)
Gravity (m/s^2)	8.56	7.85	-
Irradiation (S$_\odot$)	0.604	0.349	Delrez et al. (2018a)
Transit duration (min)	55.92	63.14	Delrez et al. (2018a)
Impact parameter b (R_*)	0.24	0.337	Delrez et al. (2018a)

NOTE—Using the updated stellar parameters from Kane (2018) the planetary radii are ∼3 larger and the gravities ∼7 lower than the values used by previous studies such as Lincowski et al. (2018).

Table 10. Mean surface temperature predicted with our 1D climate model (see Scheucher et al. accepted) for different main atmospheric compositions and stellar irradiations of TRAPPIST-1 e and TRAPPIST-1 f (T_{1D}). S_{D18} corresponds to the irradiation values shown in Delrez et al. (2018a) and S_{G17} corresponds to the values taken from Gillon et al. (2017). The surface temperatures predicted with various 3D models are shown for comparison (T_{3D}). The last column shows the reference of the corresponding 3D model study.

Planet	CO_2 (bar)	N_2 (bar)	CH_4 (bar)	T_{1D} (S_{D18})	T_{1D} (S_{G17})	T_{3D} (S_{G17})	Ref.
e	0.01	1	0	253	262	254	(1)
e	0.1	1	0	269	279	273	(1)
e	1	1	0	328	337	331	(1)
e	0	1	0.01	223	231	211	(2)
e	1	0	0	303	312	303	(3)
e	10	0	0	392	401	392	(3)
f	1	0	0	222	229	230	(3)
f	10	0	0	321	334	350	(3)

NOTE—(1) Wolf (2017), (2) Turbet et al. (2018), (3) Fauchez et al. (2019)

for TRAPPIST-1 e and an irradiation of 0.382 $S_\odot$ for planet f. In Table 10 we compare the mean surface temperature for different atmospheric compositions and using the irradiation from Gillon et al. (2017) and Delrez et al. (2018a). We also compare the temperatures with results from 3D studies.

1D models have difficulties to simulate the atmosphere of planets orbiting low-mass stars in synchronous rotation self-consistently (see e.g. Yang et al. 2013; Leconte et al. 2015; Barnes 2017). However, Table 9 shows that the surface temperatures predicted with our 1D model are in general agreement with the results from 3D studies. Using the stellar irradiation from Gillon et al. (2017) we overestimate the temperatures by ∼10 K for TRAPPIST-1 e. Only for the Titan-like atmosphere with 0.01 bar CH_4 and 1 bar N_2 do we predict a larger difference of 20 K. For a 10 bar CO_2 atmosphere of TRAPPIST-1 f we obtain a 16 K lower surface temperature compared to Fauchez et al. (2019). Note that we only simulate cloud-free conditions. The consideration of clouds in 1D models would likely but not always lead to a lower surface temperature (see e.g. Kitzmann et al. 2010; Lincowski et al. 2018).

3.3. *Model scenarios*

As input for the model we use the SEDs shown in Figure 6. The atmosphere in the climate module is divided into 101 pressure levels and the chemistry model into 100 altitude layers. We use the full photochemical network with 1127 reactions for 128 species.

Motivated by the fact that liquid water is a key requirement of life as we know it, we focus here on TRAPPIST-1 e and f, which are found to be favored candidates for habitability (see e.g. Wolf 2017; Turbet et al. 2018).

We simulate N_2 and CO_2-dominated atmospheres for TRAPPIST-1 e and CO_2-dominated atmospheres for TRAPPIST-1 f. Table 11 shows the assumed surface pressure, p_0, and the surface partial pressure of CO_2. N_2 serves as a fill gas for each simulation. The partial pressures of CO_2 are chosen according to the amount necessary to reach a surface temperature of ∼273 K (0.1 bar for planet e and 3.6 bar for planet f) and ∼340 K (1.0 bar for planet e and 10.8 bar for planet f). According to Wordsworth & Pierrehumbert (2013) water loss due to H_2O photolysis and hydrogen escape is expected to be weak for surface temperatures below 340 K (see also Kasting et al. 1993). For TRAPPIST-1 e we additionally use lower CO_2 partial pressures of 10^{-3} bar and 0.01 bar in order to compare with Hu et al. (2020) who predicted the composition profiles of TRAPPIST-1 e and f with a 1D photochemistry model using the 3D model output from Wolf (2017).

We assume three scenarios regarding the lower boundary condition: a wet & alive atmosphere with an ocean as well as biogenic and volcanic fluxes as on Earth, a wet & dead atmosphere with an ocean and only volcanic outgassing and a dry & dead atmosphere without an ocean and with only volcanic outgassing (see Table 11). We use the same surface pressure for all three scenarios having the same partial pressure of CO_2. Hence, depending on the amount of other species in the planetary atmosphere, such as O_2 or CO the amount of N_2 differs between the scenarios. However, a difference of the surface pressure impedes the comparison between the scenarios due to effects which are not entirely related to the atmospheric composition, such as the surface temperature, pressure broadening, CIA, the eddy diffusion profile and the H_2O profile in the lower atmosphere.

Biogenic and volcanic surface emissions are the same as measured for Earth (see Table 4). The ν_{dep} of CO and O_2 are shown in Table 5. For all other species we assume a ν_{dep} as measured for Earth (see Table 5). From Huang et al. (2018) we calculate that the net O_2 emissions into the atmosphere is $1.29{\cdot}10^{12}$ molecules cm^{-2} s^{-1} (11,030 Tg/yr) without taking into account fossil fuel combustion. To reproduce an O_2 mixing ratio of 0.21 for our Earth validation run (in Section 2.4.1) we need to set a ν_{dep} of $2{\cdot}10^{-8}$ cm s^{-1} (not shown) which is similar to the O_2 ν_{dep}=$1{\cdot}10^{-8}$ cm s^{-1} used by Arney et al. (2016).

Table 11. Scenarios assumed as input for the climate-photochemistry model to simulate the atmosphere of TRAPPIST-1 planets. The relative humidity (RH) is assumed to be constant up to the cold trap. The surface fluxes are the same as for pre-industrial Earth (see Table 4). For wet & alive and wet & dead we assume ν_{dep} for O_2 and CO according to the underlying scenario. For all other species the ν_{dep} shown in Table 5 are used. For each scenario we assume a range of CO_2 surface partial pressures. N_2 serves as a fill gas to reach the assumed surface pressure, p_0.

Scenario	Planet	CO_2 (bar)	p_0 (bar)	RH	Surface flux	O_2 ν_{dep} (cm s^{-1})	CO ν_{dep} (cm s^{-1})
Wet & alive	TRAPPIST-1 e	10^{-3}	1.001	80%	Biogenic and Volcanic (see Table 4)	$1{\cdot}10^{-8}$	$3{\cdot}10^{-2}$ ($1{\cdot}10^{-8}$)
	TRAPPIST-1 e	0.01	1.01				
	TRAPPIST-1 e	0.1	1.1				
	TRAPPIST-1 e	1.0	2.0				
	TRAPPIST-1 f	3.6	4.0				
	TRAPPIST-1 f	10.8	12.0				
Wet & dead	TRAPPIST-1 e	10^{-3}	1.001	80%	Volcanic (see Table 4)	$1.5{\cdot}10^{-4}$ ($1{\cdot}10^{-8}$)	$1.2{\cdot}10^{-4}$ ($1{\cdot}10^{-8}$)
	TRAPPIST-1 e	0.01	1.01				
	TRAPPIST-1 e	0.1	1.1				
	TRAPPIST-1 e	1.0	2.0				
	TRAPPIST-1 f	3.6	4.0				
	TRAPPIST-1 f	10.8	12.0				
Dry & dead	TRAPPIST-1 e	10^{-3}	1.001	80%	Volcanic (see Table 4)	$1{\cdot}10^{-8}$	$1{\cdot}10^{-8}$
	TRAPPIST-1 e	0.01	1.01				
	TRAPPIST-1 e	0.1	1.1				
	TRAPPIST-1 e	1.0	2.0				
	TRAPPIST-1 f	3.6	4.0				
	TRAPPIST-1 f	10.8	12.0				

NOTE—CO_2-poor atmosphere of TRAPPIST-1 e with CO_2 partial pressures of only 10^{-3} and 0.01 bar correspond to a T_{surf} for the wet & alive run of about 250 K and 260 K, respectively. CO_2 partial pressures of 0.1 bar and 3.6 bar for TRAPPIST-1 e and TRAPPIST-1 f, respectively, correspond to a T_{surf} of about 273 K for the wet & alive run. CO_2 partial pressures of 1 bar and 10.8 bar for TRAPPIST-1 e and TRAPPIST-1 f, respectively, correspond to a T_{surf} of about 340 K for the wet & alive run.
O_2 deposition is $1{\cdot}10^{-8}$ for an ocean saturated with O_2 (wet & alive) and for dry & dead conditions without effective O_2 surface sinks (Arney et al. 2016). For wet & dead conditions we assume that the ocean is either saturated or the ocean takes up the O_2 with a ν_{dep} of $1.5{\cdot}10^{-4}$ cm s^{-1} (Domagal-Goldman et al. 2014; Catling & Kasting 2017). Schwieterman et al. (2019) used a similar value of $\nu_{dep} = 1.4{\cdot}10^{-4}$ cm s^{-1} for anoxic atmospheres.
For wet & alive conditions we assume the same CO deposition of $\nu_{dep} = 3{\cdot}10^{-2}$ cm s^{-1} as on Earth (Hauglustaine et al. 1994; Sanhueza et al. 1998), which is larger than the ν_{dep} of $1.2{\cdot}10^{-4}$ cm s^{-1} calculated for anoxic wet atmospheres (Kharecha et al. 2005; Domagal-Goldman et al. 2014; Catling & Kasting 2017; Schwieterman et al. 2019). For conditions without effective CO surface sinks we use a ν_{dep} of $1{\cdot}10^{-8}$ cm s^{-1} (Kharecha et al. 2005; Hu et al. 2020).

Hence, we use the value used by Arney et al. (2016) as a lower limit for the deposition velocity of O_2. The corresponding Φ_{BOA} is $1.12{\cdot}10^{12}$ molecules cm^{-2} s^{-1} to obtain an O_2 mixing ratio of 0.21 with our Earth validation run. The escape rates of H, H_2 and O are calculated according to the parametrizations presented in Section 2.3.

4. RESULTS

4.1. *Atmospheric profiles of TRAPPIST-1 e with 0.1 bar CO_2*

In this Section we discuss the resulting atmospheric profiles of TRAPPIST-1 e assuming a 0.1 bar surface partial pressure of CO_2 in a 1 bar atmosphere. As model input we use all three TRAPPIST-1 spectra from Figure 6 and compare the resulting atmospheric composition.

Table 12. T_{surf} in K of TRAPPIST-1 e for all three scenarios with 0.1 bar CO_2 and different input SED of TRAPPIST-1.

Input SED	Wet & alive	Wet & dead	Dry & dead
W20 SED	273.1	269.6	251.5
P19 SED	272.2	268.2	250.4
L18 SED	273.7	270.9	252.7

4.1.1. *Temperature*

Figure 7 shows temperature, eddy diffusion coefficient and composition profiles for selected species for TRAPPIST-1 e with 0.1 bar CO_2. The different scenarios are distinguished by color and the different stellar input spectra are denoted by different line styles.

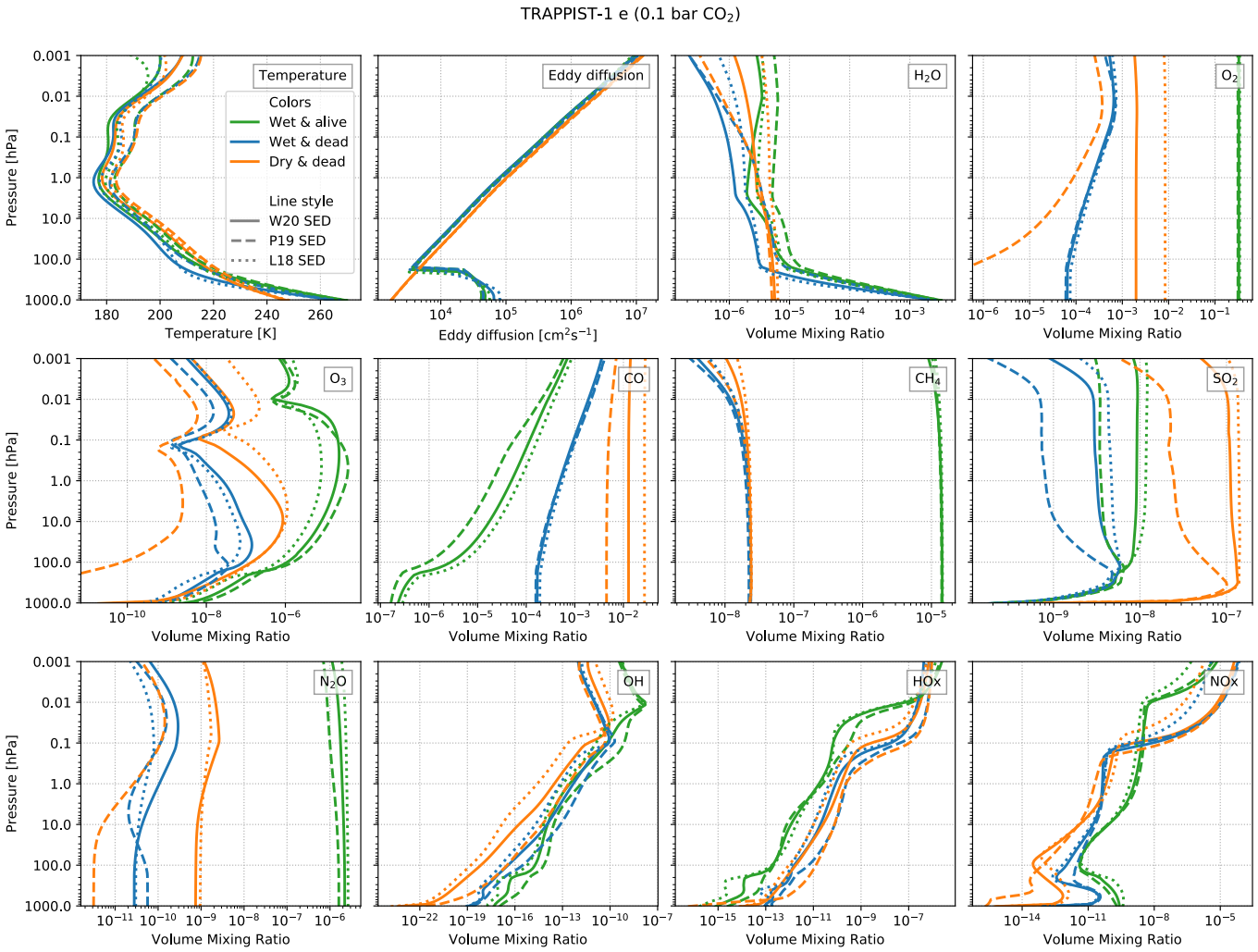

Figure 7. Temperature, eddy diffusion coefficients and composition profiles of TRAPPIST-1 e runs with 0.1 bar CO_2. Different colors represent the three scenarios considered: green for wet & alive, blue for wet & dead and orange for dry & dead. Solid lines represent results using the input TRAPPIST-1 W20 SED, dashed lines show profiles using the P19 SED and dotted lines represent the output using the L18 SED (see also Figure 6).

The temperature profiles are very similar for all runs except near the surface where the greenhouse effect of H_2O leads to larger temperatures for the wet scenarios compared to the dry & dead runs. The temperature inversion in the middle atmosphere is lacking due to weak UV absorption by O_3 (see Section 4.1.6). The wet & alive runs show the largest T_{surf} due to warming from biogenic species such as CH_4 (see Table 12). The impact of the different stellar spectra shown in Figure 6 on the planetary T_{surf} is generally small.

4.1.2. *Eddy diffusion coefficients*

For the dry scenario the eddy diffusion coefficient, K, near the surface is low and increases continuously towards higher altitudes. This is similar to the K profiles estimated for Venus and Mars (e.g. Nair et al. 1994; Krasnopolsky 2012). The wet scenarios follow a K profile which is similar to Earth with a decrease of K up to the cold trap and an increase above (Massie & Hunten 1981). This profile is also similar to that calculated by Lincowski et al. (2018) for the atmosphere of TRAPPIST-1 e, assuming an Earth-like planet covered by an ocean.

4.1.3. *H_2O*

The water profile in the lower atmosphere depends mainly on the fixed relative humidity and the temperature. For the wet scenarios the relative humidity profile is assumed to be constant at 80% in the lower atmosphere. For the dry runs only the surface H_2O is calculated with the relative humidity, otherwise the H_2O profile is determined chemically. For pressures below

1 hPa H_2O is mainly destroyed photochemically at wavelengths shorter than 200 nm and reformed via HO_x-driven (HO_x = H + OH + HO_2) oxidation of CH_4 into H_2O. The scenario which includes biogenic fluxes of the Earth as additional lower boundary condition (wet & alive) leads to significant H_2O production via CH_4 oxidation (see also Segura et al. 2005; Grenfell et al. 2013; Rugheimer et al. 2015; Wunderlich et al. 2019).

4.1.4. *CH_4*

The abundances of CH_4 are mainly driven by the surface flux. For the alive scenario we use pre-industrial (biogenic and volcanic) flux measured on Earth ($6.31{\cdot}10^{10}$ cm s^{-1}, see Table 4) and for the dead runs we use only geological sources of CH_4 ($1.12{\cdot}10^{8}$ cm s^{-1}, see Table 4). The choice of the SED has no impact on the CH_4 abundances in the lower atmosphere. For pressures below 0.1 hPa, where destruction of CH_4 is dominated by photolysis, the choice of the SED has only a weak impact on the CH_4 concentrations. As found in previous works the CH_4 abundances are increased for a planet orbiting an M-dwarf compared to a few ppm on Earth (e.g. Segura et al. 2005; Grenfell et al. 2013, 2014; Rugheimer et al. 2015; Wunderlich et al. 2019). This is mainly due to reduced sources of OH via e.g. $H_2O + O(^1D) \rightarrow 2\ OH$, where $O(^1D)$ comes mainly from O_3 photolysis in the UV. Cool stars, such as TRAPPIST-1 are weak UV emitters, favoring a slowing in the OH source reaction and less destruction of CH_4 by OH (see e.g. Grenfell et al. 2013).

In Wunderlich et al. (2019) we modelled an Earth-like planet with Earth's biofluxes around TRAPPIST-1 and found that the atmosphere would accumulate about 3000 ppm of CH_4. The much lower value of around 15 ppm suggested by this study is due to two main reasons. First, for this study we only consider the natural sources of CH_4, whereas in Wunderlich et al. (2019) we also included anthropogenic sources. CH_4 emissions similar to modern Earth would correspond to a very short period of Earth's history whereas pre-industrial emissions of CH_4 persisted for a much longer time. Second, we consider a non-zero CH_4 deposition velocity of $1.55{\cdot}10^{-4}$ cm/s, reducing the amount of CH_4 accumulated in the atmosphere. We use this measured deposition velocity of CH_4 to validate our model against Earth (see Section 2.4.1). With a zero deposition we would overestimate modern Earth amounts of CH_4 and hence, we also consider a deposition of CH_4 for the TRAPPIST-1 planets.

4.1.5. *O_2*

The alive scenario assumes a constant Earth-like O_2 flux from photosynthesis rather than a constant mixing ratio at the surface. The resulting mixing ratio for TRAPPIST-1 e with 0.1 bar CO_2 is around 35 %. The increase of O_2 compared to Earth is consistent with results of Gebauer et al. (2018a), who found that the required flux to reach a certain O_2 concentration is reduced on an Earth-like planet around AD Leo compared to the Earth around the Sun. This is due to the lower UV flux of M-dwarfs, compared to solar like stars, resulting in weaker destruction of O_2 in an Earth-like planetary atmosphere. However, for an atmosphere with about 0.35 bar O_2 forest ecosystems would be unlikely because the frequency of wildfires is expected to be increased, preventing the build-up of larger concentrations of O_2 (see e.g. Watson 1992; Kump 2008). This effect is not considered in the model.

For the dry & dead runs there is a large spread of O_2 abundances ranging from surface concentrations below 1 ppm using the P19 SED to almost 1 % using the L18 SED. This spectrum has the largest stellar FUV/NUV ratio, which was shown to favor the abiotic build-up of O_2 in CO_2-rich atmospheres as follows (see e.g. Selsis et al. 2002; Segura et al. 2007; Tian et al. 2014; France et al. 2016): CO_2 photolysis below 200 nm leads to CO and atomic oxygen. Then either atomic oxygen produces O_2 (by e.g. O + O + M $\rightarrow$ O_2 + M or O + OH + M$\rightarrow$ O_2+ H + M) or is recombined with CO via the HO_x catalysed reaction sequence, which results overall in CO_2 forming: $CO + O \xrightarrow{HO_x} CO_2$ (see e.g. Selsis et al. 2002; Domagal-Goldman et al. 2014; Gao et al. 2015; Meadows 2017). The reduced production of HO_x by H_2O destruction in the lower atmosphere for the dry & dead cases, compared to the wet & dead runs, leads to more favorable conditions for abiotic O_2 build-up. Additionally the deposition of O_2 into an unsaturated ocean, as assumed for the wet & dead cases, is stronger than the deposition onto desiccated surfaces for the dry cases (see Kharecha et al. 2005; Domagal-Goldman et al. 2014).

4.1.6. *O_3*

The production of O_3 in the middle atmosphere depends on the O_2 concentration and the UV radiation in the Schumann-Runge bands and Herzberg continuum (from about 170 nm to 240 nm). The destruction of O_3 is mainly driven by absorption in the Hartley (200 nm - 310 nm), Huggins (310 nm - 400 nm), and Chappuis (400 nm - 850 nm) bands. HO_x and NO_x destroy O_3 via catalytic loss cycles in the middle atmosphere (see e.g. Brasseur & Solomon 2006; Grenfell et al. 2013). For the scenario with constant O_2 flux of $1.21{\cdot}10^{12}$ molecules cm^{-2} s^{-1}, more O_3 is produced than for the dead runs, where O_2 is only produced abiotically. For the L18 SED

with lower UV flux between 170 and 240 nm, the O_3 layer is weaker than for the runs using the other stellar spectra. Due to enhanced abundances of O_2 compared to Earth, we find that more O_3 is produced. O'Malley-James & Kaltenegger (2017) suggested a weaker O_3 layer as on Earth, assuming an O_2 surface partial pressure of 0.21 bar.

4.1.7. *CO*

Photolysis of CO_2 in the UV produces CO and O. The dry scenario builds up more CO than the wet cases. For the alive runs with additional O_2 surface sources, the CO recombines more efficiently to CO_2 (via $CO + O \xrightarrow{HO_x} CO_2$), resulting in lower CO amounts compared to the dead runs. Additionally we assume a net deposition of CO from the atmosphere to the soil-vegetation system, reducing the amount of CO accumulated in the atmosphere (e.g. Prather et al. 1995; Sanhueza et al. 1998). As for O_2, the abundances of CO are larger for the dry & dead runs than the wet & dead runs mainly due to the assumed strong uptake of CO by the ocean for the wet scenario.

The CO mixing ratios are comparable to the results of Hu et al. (2020). For an atmosphere consisting of 1 bar N_2 and 0.1 bar CO_2 they suggest a partial pressure of CO of about 0.05 bar using a weak ν_{dep} of $1{\cdot}10^{-8}$ cm/s and a CO partial pressure of $\sim 1{\cdot}10^{-4}$ bar assuming a direct recombination reaction of O_2 and CO in the ocean. The less effective build-up of CO and abiotic O_2 due to a strong surface sink gives indirect evidence on the presence of a liquid ocean. Hence, under the simulated conditions with strong CO_2 photolysis, CO could not only serve as an "antibiosignature" gas as discussed in e.g. Zahnle et al. (2008); Wang et al. (2016); Nava-Sedeño et al. (2016); Meadows (2017); Catling et al. (2018) and Schwieterman et al. (2019) but would indirectly suggest the absence of a liquid ocean at the surface.

The largest abundances of CO for the dry scenarios are found using the L18 SED. This is due to the lower abundances of HO_x, in particular OH, which reduce the recombination of CO + O into CO_2. In turn, large amounts of HO_x, like for the dry scenario using the P19 SED, lead to low build-up of CO.

4.1.8. *SO_2*

The main source of SO_2 is volcanic outgassing, which is assumed to be equally distributed over the first 10 km of the atmosphere. For a 1 bar N_2 atmosphere with 0.1 bar CO_2, this corresponds to pressure levels below $\sim$250 hPa. The large ν_{dep} of 1 cm/s (Sehmel 1980) leads to a strong decrease of SO_2 towards the surface for all three scenarios. Due to its large solubility in water, SO_2 is deposited easily over wet surfaces, such as oceans. However, Nowlan et al. (2014) showed that over desert areas the ν_{dep} of SO_2 is approximately 0.5 cm/s, hence our value of 1 cm/s which is applied for dry cases as well may overestimate the deposition.

For the wet scenarios we assume Earth-like wet deposition following Giorgi & Chameides (1985). Most SO_2 dissolves into condensed water and is rained out of the atmosphere as sulfate. This process greatly decreases the mixing ratio of SO_2 for the wet cases but not for the dry scenarios.

The remaining SO_2 is transported upwards and is partly destroyed by photolysis. SO_2 photodissociates below 400 nm and strongest below 250 nm (e.g. Manatt & Lane 1993). Hence, for the scenarios using the P19 SED we find the strongest destruction of SO_2 above 100 hPa.

4.1.9. *N_2O*

The main N_2O source on Earth are surface biomass emissions. For the alive scenario we find concentrations of N_2O comparable to previous studies such as Rugheimer et al. (2015) and Wunderlich et al. (2019). The photodissociation of N_2O is closely related to the SED around 180 nm (e.g. Selwyn et al. 1977), leading to lower abundances of N_2O using the P19 SED.

4.2. *Transmission spectra of TRAPPIST-1 e with 0.1 bar CO_2*

Figure 8 shows the simulated transmission spectra of the TRAPPIST-1 e atmosphere scenarios with surface partial pressures of 0.1 bar CO_2, binned to a constant resolving power of R=300. The spectra are simulated by the GARLIC model taking as input the chemical and temperature profiles discussed in Section 4.1. We do not take into account the effect of clouds but we include weak extinction from aerosols (see Fig. 9).

The CO_2 absorption features are similarly strong for all runs. The wet & alive runs show strong absorption of O_3 in the VIS at around 600 nm and in the IR at 9.6 μm. The alive run with the P19 SED shows the largest O_3 features, due to the more pronounced O_3 layer in the middle atmosphere compared to the runs using the other SEDs. The spectral features of abiotic production of O_3 and O_2 for the dead runs are generally much weaker than the biogenic features. This suggests that only the O_3 feature at 9.6 μm could lead to a false positive detection of O_3.

The CH_4 feature at 2.3 μm which is visible for the alive runs overlaps in low resolution with the CO feature which occurs for the dead & dry runs. The dead runs using the W20 and L18 SEDs show much larger absorption of CO at 2.3 μm than the wet & dry runs. For

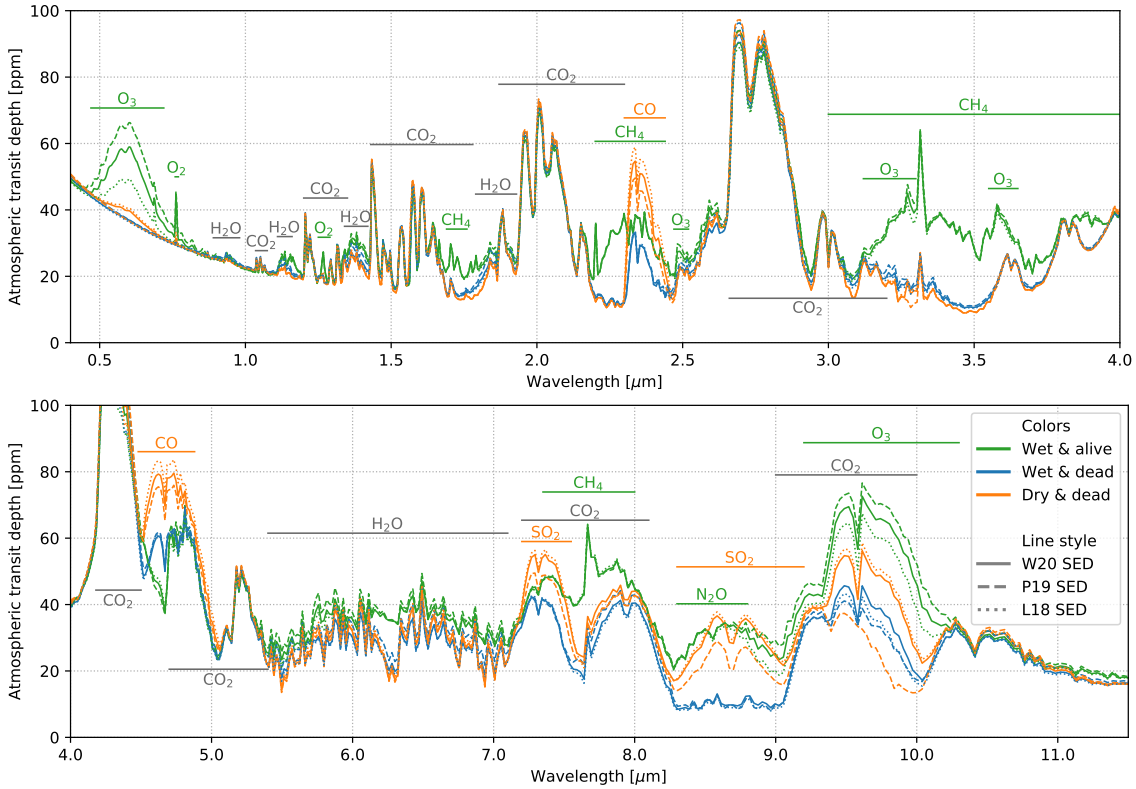

Figure 8. Simulated atmospheric features of the TRAPPIST-1 e runs with 0.1 bar CO_2, represented by cloud-free transit transmission spectra and binned to a constant resolving power of R=300 (maximum resolving power of NIRSpec PRISM at 5 μm). Important atmospheric molecular absorption bands are highlighted with horizontal lines in the color of the scenario with the strongest feature or in gray when all scenarios show a strong feature.

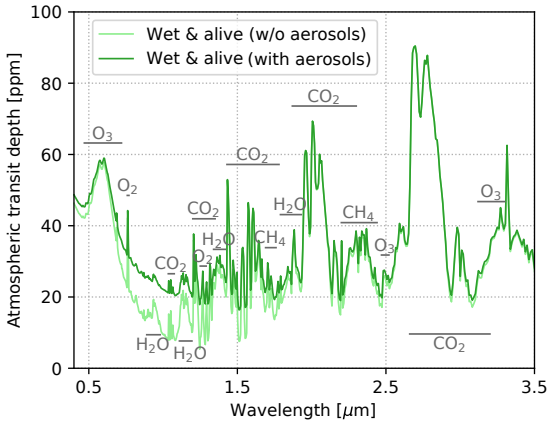

Figure 9. Simulated transmission spectrum of the TRAPPIST-1 e wet & alive run with 0.1 bar CO_2 with and without the impact of aerosol extinction.

the dead runs with the P19 SED wet and dry conditions are not clearly distinguishable due to the weak build-up of CO in the dry run (see Section 4.1.7).

Weak H_2O absorption in the lower atmosphere of the dry runs result in more pronounced spectral windows between e.g. 1.7 and 1.8 μm. The H_2O features between 5.5 and 7 μm do not show a large difference for the various scenarios since these are dominated by absorption higher up in the atmosphere, where the H_2O concentration is predominantly determined by photochemical processes and similar for all cases.

Table 13. T_{surf} in K of TRAPPIST-1 e or TRAPPIST-1 f for all scenarios and increasing amount for CO_2. The W20 SED is used as input for the atmospheric model.

Planet	CO_2 (bar)	Wet & alive	Wet & dead	Dry & dead
e	10^{-3}	245.6	245.9	238.3
e	0.01	256.7	253.3	242.7
e	0.1	273.1	269.6	251.5
e	1	335.7	331.6	281.1
f	3.6	279.6	272.7	233.5
f	10.8	330.2	327.0	258.9

4.3. *Atmospheres with increasing CO_2*

Figure 10 shows the column amount of H_2O, CO, O_2, O_3, NO_x and HO_x for all three scenarios and with increasing partial pressures of CO_2 for TRAPPIST-1 e (left) and TRAPPIST-1 f (right). Semi transparent bars represent column amounts integrated over the en-

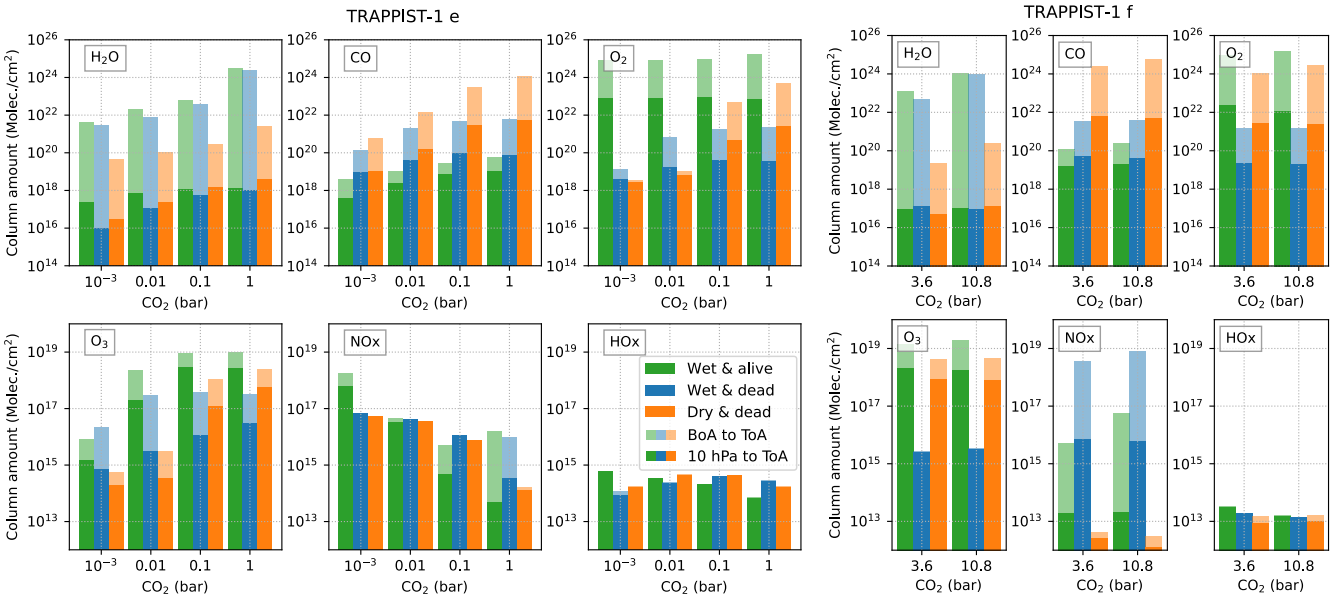

Figure 10. Column amounts (molecules cm^{-2}) of H_2O, CO, O_2, O_3, HO_x and NO_x for all atmospheric scenarios of TRAPPIST-1 e (left) and TRAPPIST-1 f (right) with increasing partial pressures of CO_2 (see also Table 11). Semi transparent bars show column amounts integrated from BoA to ToA and full filled bars show column amounts integrated from 10 hPa to ToA.

tire atmosphere whereas solid filled bars show upper column amounts integrated at pressures below 10 hPa, dominated by photochemical processes. For simulations shown in Figure 10 we use the W20 SED as input for the climate-chemistry model.

4.3.1. *H_2O*

The H_2O amount near the surface mainly depends on the relative humidity and the near surface temperature, leading to an increase of the H_2O amount towards larger CO_2 partial pressures. Whereas the dry runs show a lower H_2O content integrated over the entire atmosphere than the wet runs, at pressures below 10 hPa the three scenarios are comparable (see also Fig. 6). The T_{surf} for TRAPPIST-1 e with 1 bar CO_2 and TRAPPIST-1 f with 10.8 bar CO_2 is $\sim$ 340 K for the wet runs. While the total H_2O amount increases for an increasing T_{surf}, the increase in the upper atmospheric column is much less, which suggests that tropospheric climate is difficult to elucidate from observing middle atmosphere H_2O. Further, the mixing ratio below 10^{-5} (see Fig. 7) suggests that H_2O loss due to H_2O photolysis and hydrogen escape is expected to be weak for CO_2-rich atmospheres according to Wordsworth & Pierrehumbert (2013).

4.3.2. *CO*

As discussed in Section 4.1 dry & dead conditions favor an increase in atmospheric CO compared to the wet runs. With increasing CO_2 this effect is strengthened due to the enhanced CO_2 photolysis for intermediate CO_2 amounts. For CO_2 partial pressures of 1 bar there is only weak increase of CO column amounts compared to the atmosphere with 0.1 bar CO_2, if the ν_{dep} of CO is $1{\cdot}10^{-8}$ cm/s. For TRAPPIST-1 f runs with 90% CO_2 there is only weak increase of CO compared to the TRAPPIST-1 e run with 50% CO_2 (1 bar partial pressure of CO_2). This is consistent with results of Hu et al. (2020). They suggest, that in CO_2-rich atmospheres of TRAPPIST-1 e a nonzero deposition velocity of $1{\cdot}10^{-8}$cm s^{-1} leads to a maximum build-up of CO of around 0.05 bar.

For the wet scenarios we assume a much faster deposition of CO due to uptake of the ocean and/or vegetation. The fact that the amount of HO_x is approximately the same for dry and wet surface conditions (see Fig. 10), suggests that for wet atmospheres with low CO_2 the fast deposition of CO accounts for the weak accumulation of CO.

We also simulated the abundances of CO and O_2 for the wet scenarios assuming that the deposition of CO and O_2 into an ocean is weak (see Fig. 11). We find that the concentrations of CO would be equally high for wet & dry conditions. Only for the CO_2-dominated atmosphere of TRAPPIST-1 f more CO would be present in the dry run compared to the wet runs.

4.3.3. *O_2*

For the alive scenario the abundance of O_2 is mainly driven by the biogenic surface flux, which is equally strong in all alive runs. Due to the high FUV/NUV ratio for TRAPPIST-1 we expect that significant amounts of

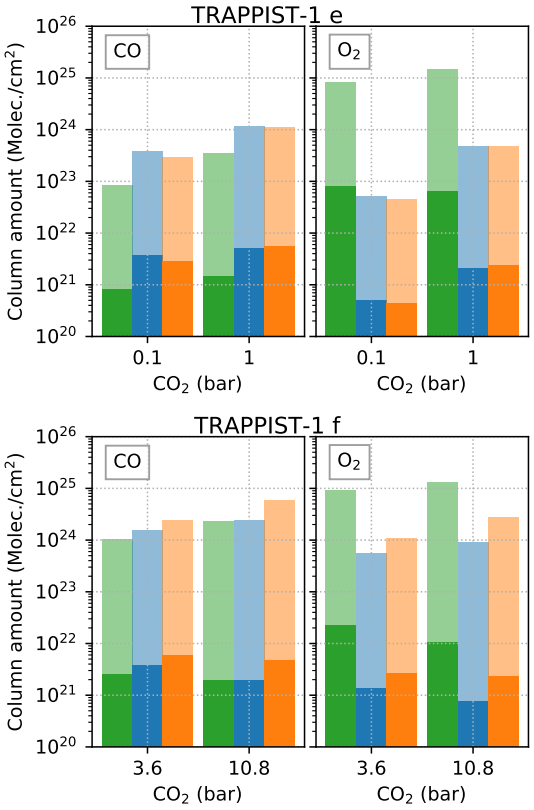

Figure 11. Same as Figure 10 but with a $\nu_{\rm dep} = 1{\cdot}10^{-8}$ cm/s for O_2 and CO, assuming that the wet runs have an ocean saturated with these gases and the biosphere is not an effective sink for CO. Only O_2 and CO are shown because the other species show similar abundances to Figure 10.

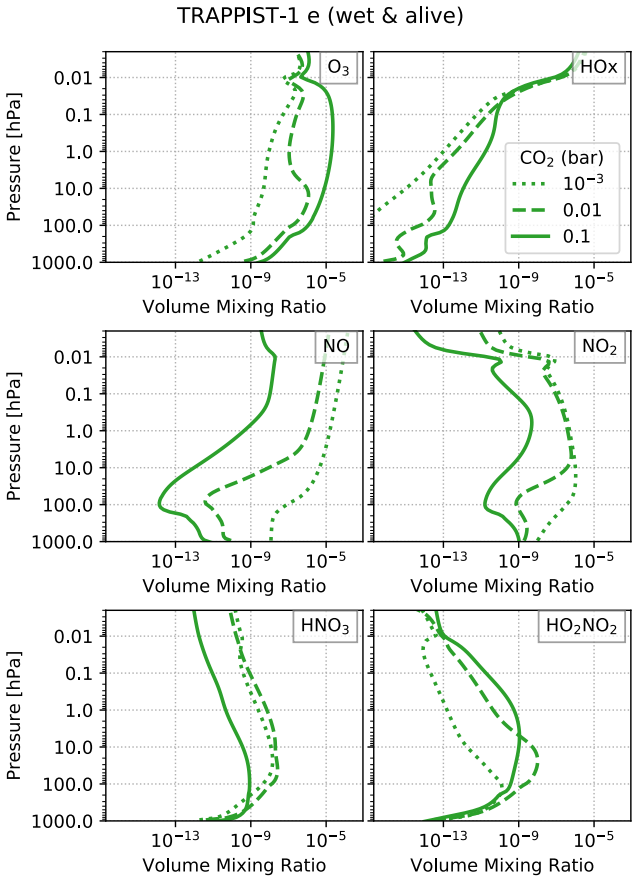

Figure 12. O_3 and related composition profiles of TRAPPIST-1 e wet & alive runs with 10^{-3} bar CO_2 (dotted line), 0.01 bar CO_2 (dashed line) and 0.1 bar CO_2 (solid line).

O_2 are produced abiotically from CO_2 photolysis. The potentially false positive detection of O_2 in CO_2 atmospheres was already discussed by several studies (e.g. Selsis et al. 2002; Segura et al. 2007; Harman et al. 2015; Meadows 2017). Figure 7 shows that the abundances of abiotic O_2 increase for dry CO_2-dominated atmospheres but are always lower than expected from a biosphere similar to the Earth. On the other hand for wet conditions without a biosphere much less abiotic O_2 is accumulated in a CO_2-dominated atmosphere. This means that weak biogenic O_2 flux would not be distinguishable from a dry N_2 atmosphere with at least 0.1 bar CO_2.

4.3.4. *O_3, NO_x and HO_x*

The three scenarios show a different O_3 behaviour with increasing CO_2 (see Fig. 10). The alive run with the lowest amount of CO_2 accumulates large amounts of NO_x, destroying most of the O_3. With increasing abundances of CO_2, the temperature increases (see Table 13) and more H_2O evaporates. This leads to more HO_x near the surface, more removal of NO_x into reservoirs such as HO_2NO_2 and less catalytic destruction of O_3 by NO_x (see Fig. 12).

For the dead runs the O_3 is produced abiotically and increases for atmospheres with more CO_2. The dry & dead runs have rather low concentrations of NO_x and HO_x for CO_2-dominated atmospheres, which suggests a weak gas-phase effect upon O_3 for these species. In contrast, the wet & dead conditions lead to a build-up of NO_x for TRAPPIST-1 f with 90% CO_2 near the surface, resulting in very low O_3 abundances in the lower atmosphere.

4.4. *Transmission spectra for increasing CO_2*

Figure 13 shows the simulated atmospheric appearance of TRAPPIST-1 e during primary transit for the three scenarios and for increasing amounts of CO_2. Several molecular features distinguish the alive run with 10^{-3} bar CO_2 from the dead runs. Features from CH_4, O_2 and N_2O are present due to the assumed biogenic flux. Strong CH_4 features are especially prevalent in

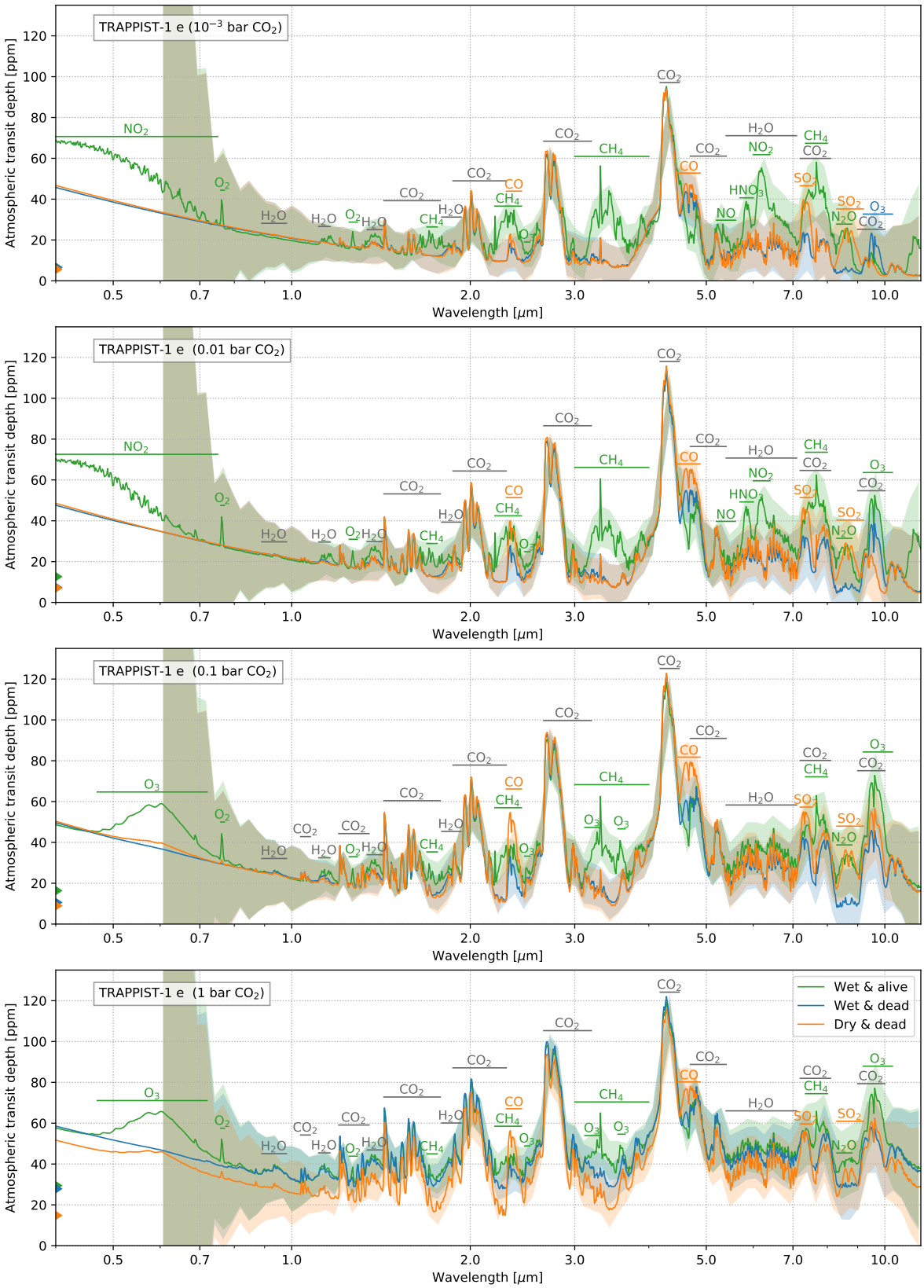

Figure 13. Simulated atmospheric features of TRAPPIST-1 e runs, represented by cloud-free transit transmission spectra and binned to a constant resolving power of R=300 (maximum resolving power of NIRSpec PRISM at 5 μm). Individual plots from top to bottom show atmospheres with increasing partial pressures of CO_2. Shaded regions represent the one sigma error of 30 co-added transit observations with JWST NIRSpec PRISM and MIRI LRS, binned to R=30 (minimum resolving power of NIRSpec PRISM at 1 μm). Important atmospheric molecular absorption bands are highlighted with horizontal lines in the color of the scenario with the strongest feature or in gray when all scenarios show significant features. Coloured triangles indicate minimum atmospheric transit depth of each scenario.

Earth-like atmospheres with low UV environments in the habitable zone around M-dwarfs (e.g. Segura et al. 2005; Rauer et al. 2011; Wunderlich et al. 2019). Additionally we find a strong NO_2 feature in the VIS as well as NO_2, NO and HNO_3 features between 5 and 7 μm due to the large amounts of these species in cold, CO_2-poor alive runs (see Fig. 12). These features are found to be present also for strong flaring conditions with cosmic-ray-induced amounts of NO_2 (see e.g. Tabataba-Vakili et al. 2016; Scheucher et al. 2018, 2020). The typical O_3 band around 9.6 μm is absent due to the large abundances of NO_x species, which can destroy O_3 catalytically.

The dead runs with low CO_2 abundances show little spectral differences between wet and dry scenarios. Only SO_2 features around 7.5 and 8.5 μm and weak CO bands around 2.3 μm and 4.7 μm distinguish the dry & dead run from the wet & dead run. With increasing CO_2 the larger abundances of CO for dry & dead conditions lead to stronger CO absorption bands and clearly separate dry from wet runs. The presence of the CO bands for CO_2-rich atmospheres was also shown by e.g. Meadows (2017) and Schwieterman et al. (2019).

For CO_2 partial pressures of 0.1 bar and above, NO_x is reduced and its spectral features do not appear in the transmission spectrum. O_3 abundances are increased and molecular bands show up in the VIS and at 9.6 μm. The CH_4 abundances are very similar for all runs and hence the CH_4 absorption at 2.3 μm and 3.3 μm for a 1 bar CO_2 should be as strong as for a CO_2-poor atmosphere. However, the increase in CO_2 abundances lead to larger lower atmosphere temperatures, hence more H_2O in this region. Since H_2O absorbs over a wide wavelength range this results in an increase in the offset of the entire spectrum (see e.g. Turbet et al. 2019), reducing the CH_4 features relative to the overall absorption. This is also suggested by Table 14, showing the baseline of TRAPPIST-1 e transmission spectra from Figure 13.

The most promising candidates for distinguishing the three scenarios from each other are the CH_4 features, which are just evident in the alive runs as well as strong CO bands for the dry runs. Absorption of CH_4 and CO features overlap at 2.3 - 2.5 μm, which could inhibit their separation. A simultaneous observation of CH_4 at 3.3 μm is therefore required as well as measurements of CO at 4.6 μm. Using JWST NIRSpec PRISM covers 0.60 - 5.30 μm, however TRAPPIST-1 is close to the saturation limit of NIRSpec PRISM (J < 10.5), resulting in a low duty cycle (see e.g. Batalha & Line 2017). We do not consider a partial saturation strategy to improve the duty cycle as suggested by Batalha et al. (2018). NIRSpec G235M only covers 1.66 - 3.12 μm, hence would not be suitable for separating CH_4 and CO. Another possibility to disentangle both features is by observing individual lines with high resolution spectroscopy (HRS). Figure 14 shows the simulated transmission spectra of the TRAPPIST-1 e runs with 0.1 bar CO_2, binned to the resolution of ELT HIRES (R=100,000). Since the position of the lines relative to each other differ between CO and CH_4 one could use the cross-correlation technique to determine which absorber causes the spectral lines or even if both species are present.

The transmission spectra of the TRAPPIST-1 f atmospheres show similar spectral features to those of TRAPPIST-1 e with 1 bar CO_2 (see Figure 15).

Table 14. Minimum atmospheric transit depth, t_{min} (ppm) and corresponding λ (μm) of the transmission spectra of TRAPPIST-1 e for all three scenarios and different amount of CO_2. t_{min} is calculated for a constant R of 300 in the NIRSpec PRISM wavelength range (0.6 - 5.3 μm).

	Wet & alive		Wet & dead		Dry & dead	
CO_2 (bar)	t_{min} (ppm)	λ (μm)	t_{min} (ppm)	λ (μm)	t_{min} (ppm)	λ (μm)
10^{-3}	9.44	3.06	6.51	3.51	6.39	3.51
0.01	12.63	2.14	7.39	3.51	7.11	3.51
0.1	16.37	1.51	10.59	3.51	8.96	3.51
1	29.44	1.25	27.86	2.24	14.84	2.24

NOTE—t_{min} depends on R and the considered wavelength range.

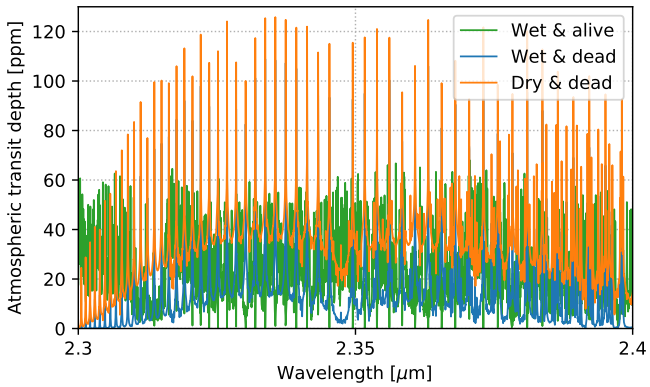

Figure 14. High resolution transmission spectra of TRAPPIST-1 e runs with 0.1 bar CO_2 with a resolving power of R=100,000, appropriate for the ELT HIRES. Green line: CH_4 features of the wet & alive run. Blue lines: CO features of the wet & dead run. Orange line: CO features of the dry & dead run. Absorption from species other than CO or CH_4 are subtracted from the spectrum.

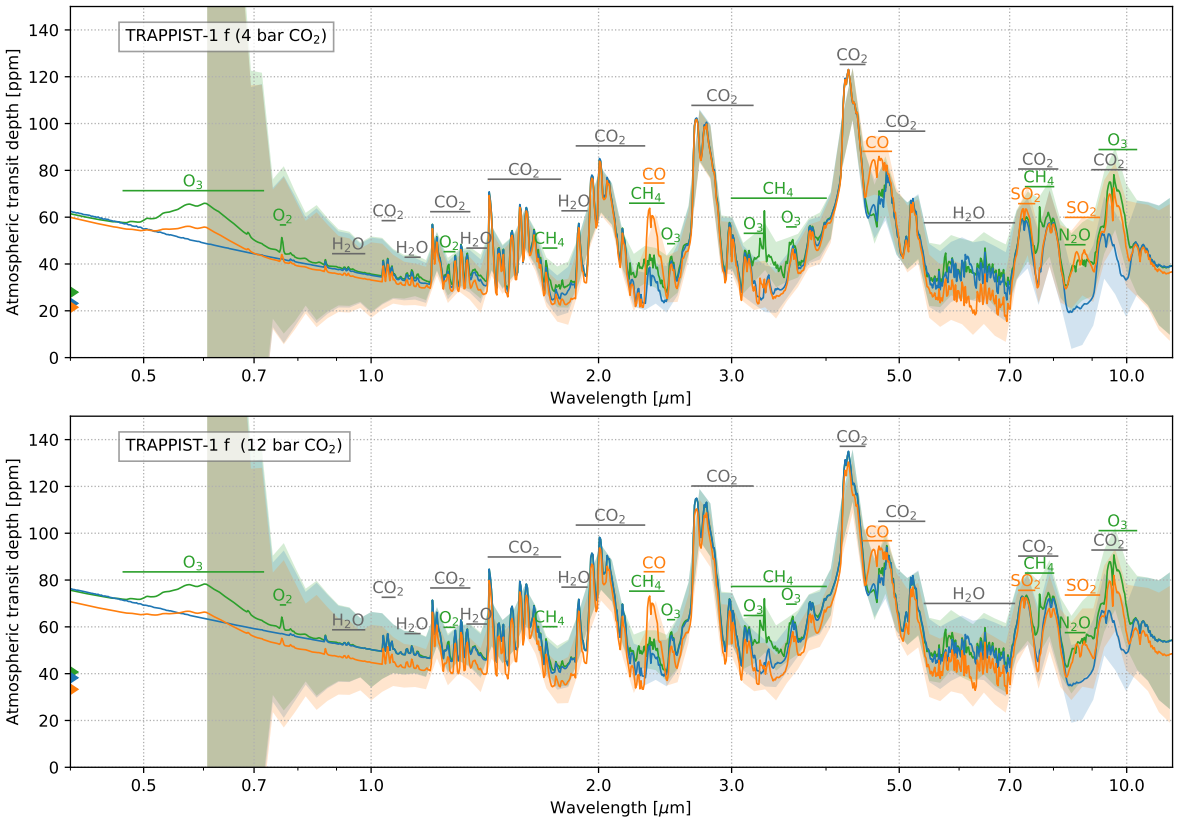

Figure 15. Same as Figure 13 but for TRAPPIST-1 f runs.

4.5. *Detectability of spectral features*

We determine the required number of transits necessary to detect a spectral feature (S/N = 5) with JWST NIRSpec or JWST MIRI. We bin the spectral data until the optimal value is found, leading to the lowest required number of transits. Binning the data decreases the noise contamination but if the binned wavelength range is too large, molecular absorption bands and atmospheric windows overlap, leading to a cancellation of the spectral feature. Due to the unknown systematic error when binning the synthetic spectral data we assume only white noise. This gives an optimistic estimation on the detection feasibility of the JWST. Additionally we estimate the number of transits required to detect spectral absorption lines with ELT HIRES using the cross correlation technique without binning the spectral data (see Section 2.6).

4.5.1. *CO_2*

Table 15 shows the number of transits needed to detect selected spectral features for all three atmospheric scenarios of TRAPPIST-1 e with 0.1 bar CO_2. For all the calculations we assume cloud-free atmospheric conditions with weak extinction from aerosols (see Eq. (3)).

With JWST NIRSpec G395M/F290LP only about 5 transits are needed to detect the 4.3 μm CO_2 feature in a cloud-free atmosphere. About twice as many transits are required to detect CO_2 with NIRSpec PRISM. This result is in agreement with other studies such as Fauchez et al. (2019), who showed that the CO_2 at 4.3 μm of a 1 bar CO_2 atmosphere of TRAPPIST-1 e would be detectable with JWST NIRSpec PRISM by co-adding 9 transits without the existence of clouds. When taking clouds into account, they suggested that 19 transits are required to detect CO_2. For a ground-based telescope such as ELT at wavelengths longer than 4 μm, the noise contribution from the Earth's atmosphere leads to very low S/N. The 2.7 μm feature of CO_2 is not observable with ELT. Hence, only the CO_2 feature around 2.0 μm might be detectable with ELT HIRES in ~30 transits.

The molecular bands for CO_2 do not greatly increase when increasing the abundances of CO_2 from 10^{-3} bar to 1 bar, hence also the number of transits needed to reach the same S/N of 5 are similar for all runs (see Fig. 16). It was shown by Barstow et al. (2016) that even the Earth and a 1 bar Venus-like atmosphere would show similar CO_2 features, which complicates the determination of the underlying atmospheric main composition by retrieval methods.

Table 15. Number of transits required to detect spectral features with an S/N of 5 in a cloud-free TRAPPIST-1 e atmosphere with 0.1 bar CO_2 using LRS with JWST NIRSpec or JWST MIRI and HRS with ELT HIRES. For LRS, λ corresponds to the central wavelength of the spectral feature whereas for HRS the considered wavelength range is given. For JWST NIRSpec the filter with the largest S/N for the spectral feature is considered (see Table 8 and Figure 5). For potentially detectable features the required number of transits using JWST NIRSpec PRISM is given in parenthesis. Numbers below 30 are highlighted in bold face.

Telescope	Specie (λ)	Wet & alive	Wet & dead	Dry & dead
JWST	CO_2 (4.3 μm)	**5 (11)**	**4 (9)**	**4 (8)**
ELT	CO_2 (1.8-2.3 μm)	33	**28**	**26**
JWST	H_2O (1.4 μm)	170	107	100
ELT	H_2O (1.3-2.0 μm)	1224	1424	865
JWST	CH_4 (3.3 μm)	60 (60)	-	-
ELT	CH_4 (2.1-2.5 μm)	**26**	7,434	>10,000
JWST	CO (2.35 μm)	-	114	**19** (57)
ELT	CO (2.3-2.45 μm)	437	105	42
JWST	O_3 (9.6 μm)	124	255	258
ELT	O_3 (3.4-3.7 μm)	4,024	>10,000	>10,000
JWST	O_2 (1.27 μm)	3,012	-	-
ELT	O_2 (1.24-1.3 μm)	910	>10,000	>10,000
JWST	SO_2 (7.35 μm)	-	-	146
ELT	SO_2 (3.9-4.1 μm)	-	-	>10,000
JWST	N_2O (8.5 μm)	1,292	-	-
ELT	N_2O (2.1-2.3 μm)	951	-	-

NOTE—The ETC for the ELT does not include the wavelength range 2.9-3.4 μm which will be covered by METIS (Brandl et al. 2016). Since O_3 absorbs in the L-band we might overestimate the number of transits required to detect O_3.

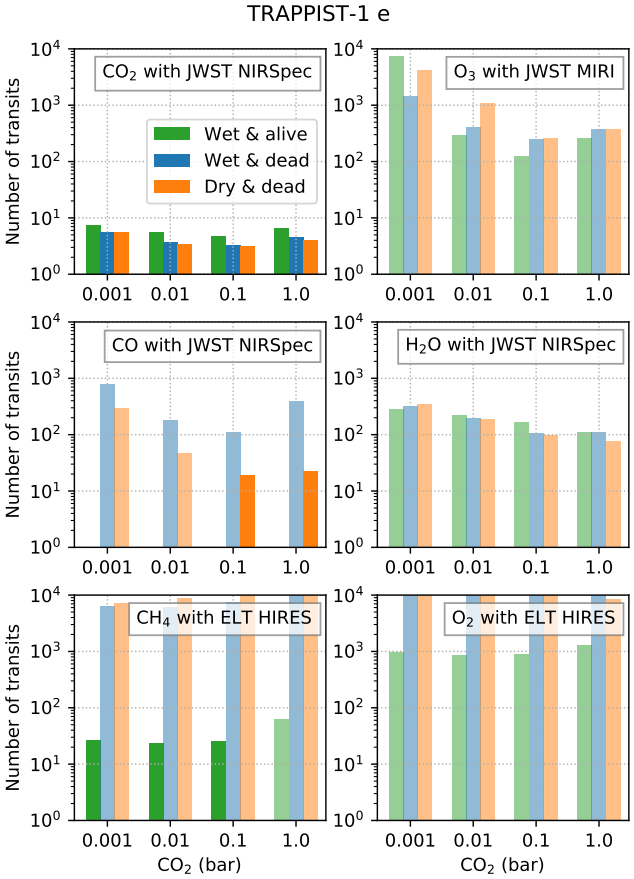

Figure 16. Number of transits required to reach an S/N of 5 for the corresponding spectral features of CO_2 at 4.3 μm, O_3 at 9.6 μm, CO at 2.35 μm and H_2O at 1.4 μm with JWST NIRSpec (upper and middle panel) and CH_4 from 2.1 to 2.5 μm and O_2 from 1.24 to 1.3 μm with ELT HIRES (lower panel) in a cloud-free atmosphere of TRAPPIST-1 e. The x-axes correspond to the increasing partial pressures of CO_2. Full filled bars: required number of transits is below or equal 30. Semi transparent bars: required number of transits is larger than 30.

4.5.2. *H_2O*

A larger CO_2 partial pressure warms the lower atmosphere, leading to more H_2O evaporation in the case of a liquid reservoir. This leads to a more opaque lower atmosphere and an increase in the measured planetary radius (see e.g. von Paris et al. 2011; Madhusudhan & Redfield 2015). In contrast, in the photochemical regime, H_2O is not greatly increased for warmer surface conditions (see Fig. 10). The effect of the radius increase is much weaker for dry atmospheres, leading to a better detectability of H_2O for dry surface conditions. However, the H_2O spectral features are too weak in all simulated atmospheres of TRAPPIST-1 e and TRAPPIST-1 f to allow for a detection with JWST NIRSpec. This was also concluded by Fauchez et al. (2019) who found that about 150 transits are required to detect H_2O in a cloud-free 1 bar CO_2 atmosphere of TRAPPIST-1 e with JWST.

Most H_2O bands in the NIR overlap with CH_4 absorption features. This could cause a false positive detection of H_2O for large abundances of CH_4 (see e.g. Wunderlich et al. 2019). The cross-correlation technique could disentangle H_2O from CH_4 but we find that by using the largest ~500 H_2O lines about ~1000 transits would be needed to detect H_2O with ELT HIRES.

4.5.3. *CH_4*

In low CO_2 atmospheres with biogenic surface fluxes the number of CH_4 lines which we identify is much larger than the H_2O lines, enabling a detection of CH_4 with less than 30 transits using ELT HIRES. The detection

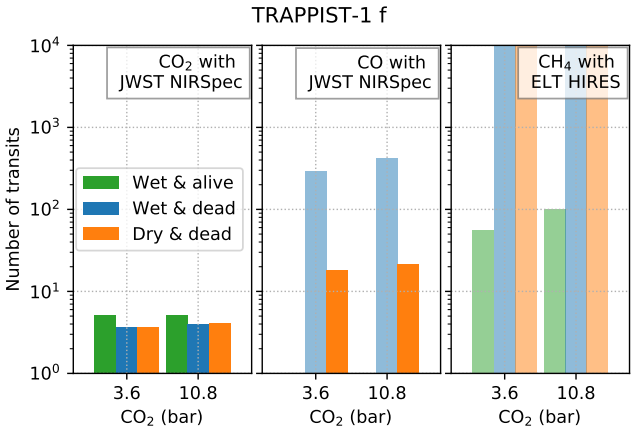

Figure 17. Number of transits required to reach an S/N of 5 for the corresponding spectral features of CO_2 at 4.3 μm and CO at 2.35 μm with JWST NIRSpec (left and center) and CH_4 from 2.1 to 2.5 μm with ELT HIRES (right) in a cloud-free atmosphere of TRAPPIST-1 f. The x-axes correspond to the increasing partial pressures of CO_2. Full filled bars: required number of transits is below or equal 30. Semi transparent bars: required number of transits is larger than 30.

of the simulated levels of CH_4 would be challenging with JWST NIRSpec.

In contrast to the alive runs, no CH_4 feature is detectable for the dead runs with only geological sources of CH_4. However, since the ability to detect CH_4 mainly depends on the assumed surface flux, which could be weaker for a potential biosphere on an M-dwarf planet (e.g. Cui et al. 2017) or stronger for enhanced volcanic outgassing of CH_4, the detection or non-detection of CH_4 alone would not confirm or rule-out the existence of a biosphere (see also Krissansen-Totton et al. 2018b).

4.5.4. *CO*

About 10% of CO_2 are needed to produce enough CO photochemically to enable a detection of its molecular absorption feature at 2.35 μm in a cloud-free atmosphere with JWST NIRSpec G235M if surface sinks of CO are inefficient. For the wet scenarios, with significant CO uptake by an ocean or a biosphere, results suggest, that CO would not be detectable, even for a CO_2-dominated atmosphere. The CO feature at 4.6 μm overlaps with the CO_2 absorption, requiring a retrieval analysis to disentangle both signals. Only about 10 transits are needed to detect the 4.6 μm band with JWST. The G395M filter of JWST would be favorable because the CO_2 band at 4.3 μm and the CO feature at 4.6 μm could be observed simultaneous.

The CO feature at 2.3 μm does not overlap with other strong absorption features in the transmission spectrum of the dry scenarios. However, 19 transits are required to detect the CO feature at 2.3 μm (see Table 15), twice as many as for the detection of the 4.6 μm CO feature. The detection of CO with the cross correlation technique has been shown to be feasible for gas giants exoplanets (see e.g. de Kok et al. 2013; Brogi et al. 2014). We find that the detection of CO would require about 40 transits with ELT HIRES in a dry, CO_2-rich, cloud-free atmosphere of TRAPPIST-1 e and f.

4.5.5. *Other molecules*

Results suggest, that no other molecular absorption features would be observable with JWST or ELT for the atmospheres considered here. Even a detection of the strong NO_2 feature around 6.2 μm in an alive CO_2-poor atmosphere (see green line in top panel of Fig. 13) would require around 50 transits with JWST MIRI (not shown). The O_3, SO_2 and N_2O features lie in a spectral region where the stellar flux is too low to allow high S/N. The O_2 feature is not strong enough for a detection with JWST NIRSpec. As also suggested by Rodler & López-Morales (2014) we find that the 1.27 μm band is more favorable than the 0.76 μm band for detecting O_2 in a planetary atmosphere around a very late M-dwarf. We find that with ELT over 900 transits are required to detect O_2 by cross-correlating the lines between 1.24 and 1.3 μm, assuming an average throughput of 10% for ELT HIRES. This is consistent with the results of Rodler & López-Morales (2014), who suggested that hundreds of transits are needed to detect O_2 in the atmosphere of Earth around an M7 star at a distance similar to TRAPPIST-1 with ELT using a high resolution spectrograph with a throughput of ∼20% (see Origlia et al. 2010).

4.5.6. *SPECULOOS targets*

With a distance of only 12.4 pc from the Sun, TRAPPIST-1 is one of the closest late-type M-dwarfs. However, we show that for the simulated atmospheres, only CO_2 would be potentially detectable within ∼10 transits. To further characterize the atmosphere of the planets observing the K-band with HRS might allow to determine whether a spectral feature around 2.3 μm can be attributed to absorption from CH_4 or CO. Our results suggest, that for a dry & dead atmosphere of TRAPPIST-1 e about 40 transits are required to detect CO with ELT HIRES. To detect an Earth-like O_2 feature with the same number of transits, a host star similar to TRAPPIST-1 is required at ∼7 pc or less (see Rodler & López-Morales 2014; Serindag & Snellen 2019).

The Search for habitable Planets EClipsing ULtracOOl Stars (SPECULOOS; Delrez et al. 2018b) is a ground-based transit survey which is looking for Earth-sized exoplanets around the nearest late M-dwarfs to

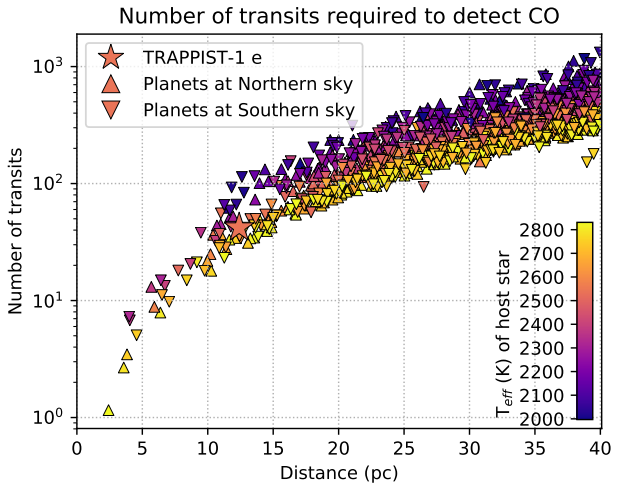

Figure 18. Number of transits required to detect CO with the cross correlation technique between 2.3 - 2.45 μm with ELT (Southern sky) or TMT (Northern sky) in the atmosphere of hypothetical planets with the same properties as TRAPPIST-1 e but around SPECULOOS targets. We assume that the atmosphere of all planets is that of the 0.1 CO_2 run with dry & dead conditions. The considered planetary atmospheric spectrum assumes cloud-free conditions.

brown dwarfs. Figure 18 shows the number of transits required to detect CO with the cross-correlation technique using TMT (Northern Sky) or ELT (Southern sky), assuming a hypothetical planet with the same properties as TRAPPIST-1 e around each member of the target list of SPECULOOS with a $T_{\rm eff}$ of at least 2000 K (see Gillon et al. 2020). The assumed atmospheric spectral feature is the same as in the dry scenario with 0.1 bar CO_2.

There are only 13 stars within a distance of 7 pc ($T_{\rm eff}$ >2000 K), where the atmospheric O_2 feature of a hypothetical terrestrial planet would be detectable within 40 transits according to Rodler & López-Morales (2014). However, non-LTE effects in the O_2 1.27 μm band may prevent a detection (López-Puertas et al. 2018). Figure 18 suggests that more targets exists for which the CO feature could be detected. For late M-dwarfs (2400 K $< T_{\rm eff} <$ 2800 K) CO could be detected up to ∼12pc using ELT or TMT by co-adding 30 transits. Early L-dwarfs ($T_{\rm eff}$ <2400 K) only have slightly smaller stellar radius than late M-dwarfs but are much fainter, resulting in a low S/N and more transits are required to detect atmospheric molecular features with transmission spectroscopy.

5. DISCUSSION

With our climate-photochemistry model, 1D-TERRA, we simulated potential atmospheres of TRAPPIST-1 e and TRAPPIST-1 f. We determined the composition of the planetary atmospheres, assuming N_2 and CO_2-dominated atmospheres with wet and dry surface conditions. We did not consider O_2-rich atmospheres, accumulated from H_2O photolysis during the pre-main sequence phase of TRAPPIST-1 (see e.g. Wordsworth & Pierrehumbert 2014; Luger & Barnes 2015; Bolmont et al. 2016). However, an Earth-like biogenic flux of O_2 is considered and O_2 can also build up abiotically via CO_2 photolysis. For detailed discussion of the potential composition and transmission spectra of O_2-dominated atmospheres from H_2O photolysis we refer to Lincowski et al. (2018).

The main goal of our study was to investigate which spectral features of wet or dry planets in the habitable zone could be detectable with the upcoming JWST and ELT. We identify three species which could be detectable in a cloud-free atmosphere of TRAPPIST-1 e or f by co-adding less than 30 transits: CO_2, CH_4 and CO. Under the assumed boundary conditions, CO_2 would be detectable with JWST and ELT with about 10 transits. This is also consistent with several other studies investigating the detectability of the atmospheric features of the TRAPPIST-1 planets (Morley et al. 2017; Batalha et al. 2018; Krissansen-Totton et al. 2018a; Wunderlich et al. 2019; Lustig-Yaeger et al. 2019; Fauchez et al. 2019). However, for N_2-dominated atmospheres the uncertainties of the retrieved CO_2 abundances are up to 2 orders of magnitude when co-adding 10 transits (see Batalha et al. 2018; Krissansen-Totton et al. 2018a).

The effect of clouds and hazes is not considered in the model and we only consider weak extinction by aerosols for the simulation of the transmission spectra. We do not expect a large impact on the chemical composition when considering thin cloud or haze layers (see Venus validation, Figure 4). However, the presence of clouds can significantly reduce the detectability of molecular spectral features (see e.g. Kitzmann et al. 2011a,b; Vasquez et al. 2013; Benneke & Seager 2013; Bétrémieux & Kaltenegger 2014; Bétrémieux & Swain 2017; Moran et al. 2018; Lustig-Yaeger et al. 2019; Fauchez et al. 2019; Komacek et al. 2020; Suissa et al. 2020). We use a similar expression to simulate the effect of aerosol absorption to Kaltenegger & Traub (2009). They conclude that the apparent radius of an atmosphere like on Earth is mainly determined by Rayleigh scattering and aerosol, H_2O and CO_2 absorption. For Earth, the inclusion of realistic cloud coverage has only a small effect on the apparent radius and hence, the detectability of spectral features.

For the wet scenarios with low CO_2 abundances and Earth-like biomass surface emissions we find that CH_4

would be detectable on TRAPPIST-1 e using the cross-correlation technique with less than 30 transits. Increasing the amount of CO_2 leads to additional greenhouse warming and more H_2O evaporated into the atmosphere. More H_2O in the lower atmosphere leads to an increase of the minimum transit depth in the transit spectrum, i.e. the observational baseline (see also Turbet et al. 2019). The strongest CH_4 feature at 3.3 μm is about 40 ppm above the baseline, when very little H_2O is present in the atmosphere. For a lower atmosphere with a relative humidity of 80% and a $T_{\rm surf}$ of ∼335 K the baseline increases by 20 ppm compared to a cold atmosphere with a $T_{\rm surf}$ of ∼245 K. Due to this effect, for CO_2-dominated atmospheres of TRAPPIST-1 e and TRAPPIST-1 f CH_4 would not be detectable for a pre-industrial Earth-like emission flux of CH_4, since this feature would be partially swamped by the baseline. For these cases the spectral appearance would not suggest the existence of a biosphere within the detection limits, i.e. it would be a false negative detection of CH_4.

Enhanced outgassing when assuming e.g. a more reducing mantle than modern Earth would need to be 2-3 orders of magnitudes larger than for modern Earth to build up as much CH_4 as for the alive scenarios (see also Ryan et al. 2006; Krissansen-Totton et al. 2018b). Since also the outgassing of CO is expected to be large for a highly reduced mantle, simultaneous detection of CO could distinguish an atmosphere with large amounts of outgassed abiotic CH_4 from an atmosphere with mainly biogenic CH_4 (see also Krissansen-Totton et al. 2018b).

The presence of large amounts of CO has been suggested to indicate the absence of life on an exoplanet (Zahnle et al. 2008; Wang et al. 2016; Nava-Sedeño et al. 2016; Meadows 2017; Catling et al. 2018). We find that the CO feature at 2.3 μm would be detectable with JWST NIRSpec for a dry atmosphere with at least 0.1 bar CO_2 by co-adding ∼20 transits (Fig. 16). In contrast to CH_4, CO would be detectable also for CO_2-dominated atmospheres due to the enhanced CO build-up from CO_2 photolysis.

The detection of CO with ELT HIRES requires twice as much transits than with JWST when assuming an average throughput of 10%. Previous studies such as Snellen et al. (2013) or Serindag & Snellen (2019) assume a mean throughput of 20% for ELT. However, to achieve this large efficiency further development of the instrument design might be necessary (see e.g. Ben-Ami et al. 2018).

For dry surface conditions, without a liquid ocean, we expect that very little CO would be deposited onto the surface. In contrast, the existence of an ocean may inhibit the build-up of substantial amounts of CO in a CO_2-rich atmosphere through catalytic cycles and an effective CO surface sink. This would lead to a non-detection of CO for wet surface conditions. However, the detection of CO in a CO_2-rich atmosphere of an M-dwarf planet could be also compatible with the presence of an ocean and a biosphere with ineffective surface sinks of CO or increased CO surface flux (Krissansen-Totton et al. 2018b; Schwieterman et al. 2019). Hence, the detection of CO does not ultimately discriminate between wet and dry surface conditions but a non-detection of CO and a simultaneous detection of CO_2 in the atmosphere of a potential habitable TRAPPIST-1 planet can hint at an effective surface sink for CO, suggesting the existence of an ocean.

As for CO, we find that abundances of SO_2 are much larger for dry surface conditions than for wet conditions. For the wet scenarios, most of the SO_2 is oxidised into highly soluble sulfate hence efficiently removed from the atmosphere by wet and dry deposition. For the dry scenarios we do not consider any wet deposition. Loftus et al. (2019) suggests that the detection of an H_2SO_4-H_2O haze layer together with SO_2 indicate that the planet does not host significant surface liquid water. The large amounts of SO_2 we find for the dry surface conditions are consistent with their study. However, the detection of SO_2 would not be feasible for any of the dry runs of TRAPPIST-1 e and TRAPPIST-1f with JWST or ELT. Furthermore, the SO_2 may form a haze layer.

For the simulated N_2 and CO_2-dominated atmospheres, one would require large observational times to detect spectral features in the atmospheres of the TRAPPIST-1 planets with JWST or ELT (see also Morley et al. 2017; Batalha et al. 2018; Krissansen-Totton et al. 2018a; Wunderlich et al. 2019; Lustig-Yaeger et al. 2019; Gillon et al. 2020).

In this study we assume white noise only when co-adding multiple transits or binning spectral data to a lower resolution than observed. This assumption may underestimate the required number of transits significantly, especially for weak spectral features (see e.g. Fauchez et al. 2019). Imaging spectroscopy concepts such as the Large UV/Optical/Infrared Surveyor (LUVOIR, The LUVOIR Team 2019) and the Habitable Exoplanet Observatory (HabEx, Mennesson et al. 2016) may provide new opportunities to observe the atmosphere of terrestrial planets (see e.g. Pidhorodetska et al. 2020). The angular separation between TRAPPIST-1 and TRAPPIST-1 e is only 2.4 milliarcseconds (mas), much smaller than for Proxima Centauri b (37 mas) (O'Malley-James & Kaltenegger 2019). This might be too small to separate the star and the planets with LUVOIR or HabEx (see also Stark et al. 2015). Hence,

transmission spectroscopy is the most promising way to constrain the atmospheric characteristics of the habitable TRAPPIST-1 planets in the next few decades.

The recent detection of H_2O absorption in the atmosphere of the habitable zone planet K2-18b is one example of how the existence of an H_2 envelope could enable the characterization of the atmosphere of potentially rocky planets (Benneke et al. 2019; Tsiaras et al. 2019). Initial observations of the TRAPPIST-1 planets showed no hint of cloud-free H_2 or helium dominated atmospheres, suggesting that atmospheres are dominated by heavier elements (de Wit et al. 2016, 2018; Wakeford et al. 2018; Burdanov et al. 2019). However, hydrogen-rich atmospheres with high-altitude clouds or hazes are also consistent with the observations of the TRAPPIST-1 planets (Moran et al. 2018). Such hydrogen-rich atmospheres of the planets would increase the scale height, leading to improved detectability of spectral features.

Table 16. Important molecular absorption features and corresponding wavelength in μm of the simulated transmission spectra of TRAPPIST-1 e for all three scenarios and with CO_2-poor (10^{-3}, 0.01 bar) and CO_2-rich (0.1, 1 bar) atmospheres. In black: strong spectral features, in gray: weak spectral features.

Scenario	CO_2-poor (10^{-3}, 0.01 bar)	CO_2-rich (0.1, 1 bar)
	O_2 (0.76, 1.27)	O_2 (0.76, 1.27)
	O_3 (9.6)	O_3 (0.6, 9.6)
Wet	CH_4 (2.3, 3.3, 7.7)	CH_4 (2.3, 3.3, 7.7)
& alive	NO_2 (below 0.7, 3.45, 6.2)	-
	NO (5.3)	-
	HNO_3 (5.85)	-
	N_2O (8.5)	-
Wet	O_3 (9.6)	O_3 (9.6)
& dead	CO (2.35, 4.6)	CO (2.35)
	-	O_2 (0.76, 1.27)
Dry	-	O_3 (0.6, 9.6)
& dead	CO (2.35, 4.6)	CO (2.35, 4.6)
	SO_2 (7.35, 8.7)	SO_2 (7.35, 8.7)

6. SUMMARY AND CONCLUSION

We introduced and validated our new chemical network, part of our updated 1D coupled climate-photochemistry model (1D-TERRA). The model is capable of simulating the atmosphere of terrestrial planets over a wide range of temperatures and pressures. Our chemical network is based on those presented by Hu et al. (2012) and Arney et al. (2016). Additionally we added chlorine chemistry and extended the sulphur chemistry with chemical reactions listed in Zhang et al. (2012), in order to simulate Venus-like atmospheres. We showed that the model is able to reproduce modern Earth as well as CO_2-dominated atmospheres such as present on modern Mars and Venus. The resulting composition profiles are consistent with observations and other photochemical models, dedicated to model the atmosphere of Mars (Nair et al. 1994; Krasnopolsky 2010a) and Venus (Krasnopolsky 2012; Zhang et al. 2012).

In this paper we simulated the potential atmospheres of the TRAPPIST-1 e and TRAPPIST-1 f planets assuming N_2 and CO_2-dominated atmospheres for three main scenarios regarding the lower boundary condition: first, a wet & alive atmosphere with an ocean as well as biogenic and volcanic fluxes as on Earth, second, a wet & dead atmosphere with an ocean and only volcanic outgassing and, third, a dry & dead atmosphere without an ocean and with only volcanic outgassing (see Table 11). We showed the simulated atmospheric composition and spectral appearance of TRAPPIST-1 e with 0.1 bar CO_2 using three different SEDs as input for the climate-chemistry model. To our knowledge ours is the first study which uses an SED of TRAPPIST-1 which was constructed based on measurements in the UV (Wilson et al. submitted).

Starting from an N_2-dominated atmosphere we increased the surface partial pressures of CO_2 from 10^{-3} bar for TRAPPIST-1 e up to 10.8 bar for TRAPPIST-1 f. The main results regarding the composition of the simulated atmospheres are listed below.

- The alive runs with Earth-like biogenic flux accumulate about 50% more O_2 as on modern Earth due to Earth's weaker UV environment and hence weaker O_2 sinks.

- For dry CO_2-rich atmospheres, the abiotic production of O_2 and O_3 is significant (see also Selsis et al. 2002; Segura et al. 2007; Harman et al. 2015; Meadows 2017), as expected due to the low FUV/NUV ratio of TRAPPIST-1 (Tian et al. 2014). However, the abundances of abiotic O_2 and O_3 is one order of magnitude lower than those runs with biogenic emissions. In contrast, the wet & dead scenario without biogenic emissions shows little abiotic O_2 and O_3 due to effective O_2 uptake by the ocean.

- CO can be an indirect marker of an ocean, being 100 times larger on an ocean-less world with a CO_2-rich atmosphere (see also Zahnle et al. 2008; Gao et al. 2015; Wang et al. 2016; Nava-Sedeño et al. 2016; Meadows 2017; Schwieterman et al. 2019; Hu et al. 2020).

- For dry scenarios the mixing ratio of O_2 and O_3 can differ by over two orders of magnitude and abundances of CO and SO_2 can differ by about one order of magnitude depending on the choice of the SED. For the wet scenarios the concentrations of O_3 in the middle atmosphere depend on the choice of the SED by a factor of ∼5.

- For dry scenarios the outgassed SO_2 leads to larger atmospheric concentrations than for the wet cases which include wet deposition.

We used the simulated atmospheric composition to calculate cloud-free transmission spectra of TRAPPIST-1 e for all three scenarios. Important spectral features found for the individual scenarios are listed in Table 16.

We used the transmission spectra and the TRAPPIST-1 SED from Wilson et al. (submitted) to calculate the number of transits required to detect molecular features of TRAPPIST-1 e and TRAPPIST-1 f. The results are listed below.

- The detection of CO_2 at 4.3 μm with JWST NIRSpec PRISM requires ∼10 transits assuming cloud-free conditions (similar to findings by Morley et al. 2017; Batalha et al. 2018; Krissansen-Totton et al. 2018a; Wunderlich et al. 2019; Lustig-Yaeger et al. 2019; Fauchez et al. 2019). With the cross-correlation technique using ELT HIRES the CO_2 feature around 2.0 μm might be detectable by co-adding ∼30 transits. CO_2 will be easier to detect for the dry & dead scenario due to weak absorption of H_2O and CH_4.

- For the wet & alive runs CH_4 might be detectable with ELT HIRES for the simulated cloud-free atmospheres of TRAPPIST-1 e with a surface temperature below 330 K. CH_4 is not detectable for any simulated case without biomass flux.

- O_2 is not detectable for the simulated atmospheres of TRAPPIST-1 e or TRAPPIST 1 f using the cross-correlation technique with ELT HIRES (see also Rodler & López-Morales 2014; Serindag & Snellen 2019).

- SO_2 indicates that a planet might not host significant surface liquid water. However, SO_2 is not detectable for any of the dry runs of TRAPPIST-1 e and TRAPPIST-1 f with JWST or ELT.

- CO at 2.35 μm might be detectable with JWST NIRSpec G235M for dry scenarios with weak surface deposition of CO and a CO_2 partial pressure above 0.01 bar. The detection of CO require about 60 transits with JWST NIRSpec PRISM and about 40 transits with ELT HIRES. The CO feature at 4.6 μm would be detectable with JWST but partially overlaps with CO_2 absorption. Accurate retrieval may be able to disentangle CO and CO_2 with JWST.

We conclude that the three scenarios considered for TRAPPIST-1 e might be distinguishable for cloud-free conditions by combining ∼30 transit observations with JWST NIRSpec and ELT HIRES in the K-band (2.0-2.4 μm), if the CO_2 partial pressures on top of a 1 bar N_2-dominated atmosphere are above 0.01 and below 1 bar. The alive scenario, assuming Earth-like emission of CH_4, could be identified by the detection of CH_4. The non-detection of CO suggests the existence of a surface ocean. In turn, the detection of CO suggests dry surface conditions. A detection of CO_2 and a non-detection of CO and CH_4 suggests that liquid water on the surface reduces the amount of CO in the atmosphere and that biogenic emissions of CH_4 are weak.

ACKNOWLEDGMENTS

This research was supported by DFG projects RA-714/7-1, GO 2610/1-1, SCHR 1125/3-1 and RA 714/9-1. We acknowledge the support of the DFG priority programme SPP 1992 "Exploring the Diversity of Extrasolar Planets (GO 2610/2-1)". M. L.-P. acknowledges financial support from the State Agency for Research of the Spanish MCIU through project ESP2017-87143-R, the "Center of Excellence Severo Ochoa" award to the IAA-CSIC (SEV-2017-0709), and EC FEDER funds. PCS gratefully acknowledges support by the German Aerospace Center under DLR 50 OR 1901. J.L.G. gratefully acknowledges the support of ISSI Team 464. We thank Michaël Gillon for providing the SPECULOOS target list, Franklin Mills for sending cross section data of several sulphur species and Vladimir Krasnopolsky for providing chemical profiles of Mars. The SED used is this study is based on observations made with the NASA/ESA Hubble Space Telescope, obtained from the Data Archive at the Space Telescope Science Institute, which is operated by the Association of Universities for Research in Astronomy, Inc., under NASA contract NAS 5-26555. These observations are associated with program # 15071. Support for program #15071 was provided by NASA through a grant from the Space Telescope Science Institute. We thank the anonymous referee for the helpful and constructive comments.

Software: GARLIC (Schreier et al. 2014, 2018), HITRAN 2016 (Gordon et al. 2017), MPI Mainz Spectral Atlas (Keller-Rudek et al. 2013), ESO ETC (Liske 2008), NIST (Mallard et al. 1994), S/N calculator for JWST (Wunderlich et al. 2019), 1D Climate-Chemistry model legacy (Kasting & Ackerman 1986; Pavlov et al. 2000; Segura et al. 2003; von Paris et al. 2015, and others)

REFERENCES

Ackerman, A. S., & Marley, M. S. 2001, ApJ, 556, 872

Allard, F. 2016, in SF2A-2016: Proceedings of the Annual meeting of the French Society of Astronomy and Astrophysics, 223–227

Allen, C. 1976, University of London

Allen, C. W. 1973, Astrophysical quantities

Allen, M., Yung, Y. L., & Waters, J. W. 1981, JGR: Space Physics, 86, 3617

Ångström, A. 1929, Geografiska Annaler, 11, 156

—. 1930, Geografiska Annaler, 12, 130

—. 1961, Tellus, 13, 214

Arney, G., Domagal-Goldman, S. D., & Meadows, V. S. 2018, AsBio, 18, 311

Arney, G., Domagal-Goldman, S. D., Meadows, V. S., et al. 2016, AsBio, 16, 873

Arney, G. N., Meadows, V. S., Domagal-Goldman, S. D., et al. 2017, ApJ, 836, 49

Banks, P. 1973, G. Kockarts Aeronomy Part A, Academic Press, New York

Baraffe, I., Homeier, D., Allard, F., & Chabrier, G. 2015, A&A, 577, A42

Barnes, R. 2017, CMDA, 129, 509

Baron, E., & Hauschildt, P. H. 2007, A&A, 468, 255

Barstow, J. K., Aigrain, S., Irwin, P. G., Kendrew, S., & Fletcher, L. N. 2016, MNRAS, 458, 2657

Batalha, N. E., Lewis, N. K., Line, M. R., Valenti, J., & Stevenson, K. 2018, ApJL, 856, L34

Batalha, N. E., & Line, M. R. 2017, ApJ, 153, 151

Beichman, C., Benneke, B., Knutson, H., et al. 2014, PASP, 126, 1134

Belyaev, D. A., Montmessin, F., Bertaux, J.-L., et al. 2012, Icar, 217, 740

Ben-Ami, S., López-Morales, M., Garcia-Mejia, J., Abad, G. G., & Szentgyorgyi, A. 2018, ApJ, 861, 79

Benneke, B., & Seager, S. 2013, ApJ, 778, 153

Benneke, B., Wong, I., Piaulet, C., et al. 2019, ApJ, 887, L14

Bernath, P. 2017, JQSRT, 186, 3

Berresheim, H., Wine, P., & Davis, D. 1995, Composition, chemistry, and climate of the atmosphere, 8, 251

Bertaux, J.-L., Vandaele, A.-C., Korablev, O., et al. 2007, Natur, 450, 646

Bétrémieux, Y., & Kaltenegger, L. 2014, ApJ, 791, 7

Bétrémieux, Y., & Swain, M. R. 2017, MNRAS, 467, 2834

Birkby, J., de Kok, R., Brogi, M., et al. 2013, MNRAS: Letters, 436, L35

Birkby, J. L. 2018, arXiv preprint arXiv:1806.04617

Birkmann, S. M., Ferruit, P., Rawle, T., et al. 2016, Proc. SPIE, 9904, 99040B

Bolmont, E., Selsis, F., Owen, J. E., et al. 2016, MNRAS, 464, 3728

Boone, C. D., Nassar, R., Walker, K. A., et al. 2005, Appl. Opt., 44, 7218

Bouche, J., Bauduin, S., Giuranna, M., et al. 2019, JQSRT, 106498

Bourrier, V., Ehrenreich, D., Wheatley, P., et al. 2017, A&A, 599, L3

Bouwman, A., Lee, D., Asman, W., et al. 1997, Global biogeochemical cycles, 11, 561

Brandl, B. R., Agócs, T., Aitink-Kroes, G., et al. 2016, Proc. SPIE, 9908, 990820

Brasseur, G. P., & Solomon, S. 2006, Aeronomy of the middle atmosphere: chemistry and physics of the stratosphere and mesosphere, Vol. 32 (Springer Science & Business Media)

Brion, C., Tan, K., van der Wiel, M., & van der Leeuw, P. 1979, Journal of Electron Spectroscopy and Related Phenomena, 17, 101

Brogi, M., de Kok, R., Birkby, J., Schwarz, H., & Snellen, I. 2014, A&A, 565, A124

Brogi, M., Giacobbe, P., Guilluy, G., et al. 2018, A&A, 615, A16

Brogi, M., & Line, M. R. 2019, ApJ, 157, 114

Burdanov, A. Y., Lederer, S. M., Gillon, M., et al. 2019, MNRAS, 487, 1634

Burkholder, J., Sander, S., Abbatt, J., et al. 2015, Chemical kinetics and photochemical data for use in atmospheric studies: evaluation number 18, Tech. rep., Pasadena, CA: Jet Propulsion Laboratory, National Aeronautics and Space

Catling, D. C., & Kasting, J. F. 2017, Atmospheric evolution on inhabited and lifeless worlds (Cambridge University Press)

Catling, D. C., Krissansen-Totton, J., Kiang, N. Y., et al. 2018, AsBio, 18, 709

Chameides, W., Stedman, D., Dickerson, R., Rusch, D., & Cicerone, R. 1977, Journal of the Atmospheric Sciences, 34, 143
Chan, W., Cooper, G., & Brion, C. 1993, Chemical Physics, 178, 387
Clilverd, M. A., Seppälä, A., Rodger, C. J., Mlynczak, M. G., & Kozyra, J. U. 2009, JGR: Space Physics, 114
Clough, S., Kneizys, F., & Davies, R. 1989, Atmospheric Research, 23, 229
Cui, D., Tian, F., Wang, Y., et al. 2017, AsBio, 17, 1219
de Kok, R. J., Brogi, M., Snellen, I. A., et al. 2013, A&A, 554, A82
de Wit, J., Wakeford, H. R., Gillon, M., et al. 2016, Natur, 537, 69
de Wit, J., Wakeford, H. R., Lewis, N. K., et al. 2018, Nature Astronomy, 2, 214
Delrez, L., Gillon, M., Triaud, A. H. M. J., et al. 2018a, Monthly Notices of the Royal Astronomical Society, 475, 3577
Delrez, L., Gillon, M., Queloz, D., et al. 2018b, Proc. SPIE, 10700, 107001I
Domagal-Goldman, S. D., Segura, A., Claire, M. W., Robinson, T. D., & Meadows, V. S. 2014, ApJ, 792, 90
Dong, C., Jin, M., Lingam, M., et al. 2018, Proceedings of the National Academy of Sciences, 115, 260
Duflot, V., Wespes, C., Clarisse, L., et al. 2015, Atmospheric Chemistry and Physics, 15, 10509
Encrenaz, T., Greathouse, T. K., Richter, M., et al. 2011, A&A, 530, A37
Etiope, G., & Ciccioli, P. 2009, Science, 323, 478
Fally, S., Vandaele, A., Carleer, M., et al. 2000, Journal of Molecular Spectroscopy, 204, 10
Fauchez, T. J., Turbet, M., Villanueva, G. L., et al. 2019, ApJ, 887, 194
Fedorova, A., Korablev, O., Bertaux, J.-L., et al. 2009, Icar, 200, 96
Fischer, H., Birk, M., Blom, C., et al. 2008, ACP, 8, 2151
Fleming, D. P., Barnes, R., Luger, R., & VanderPlas, J. T. 2020, ApJ, 891, 155
France, K., Loyd, R. O. P., Youngblood, A., et al. 2016, ApJ, 820, 89
Froning, C. S., France, K., Parke Loyd, R., et al. 2018, in AAS Meeting, Vol. 231
Funke, B., López-Puertas, M., García-Comas, M., Stiller, G. P., & von Clarmann, T. 2010, in Astrophysics and Space Science Proc., 181–189
Funke, B., López-Puertas, M., Gil-López, S., et al. 2005, JGR: Atmospheres, 110
Funke, B., López-Puertas, M., Stiller, G. P., Versick, S., & von Clarmann, T. 2016, ACP, 16, 8667
Funke, B., López-Puertas, M., Stiller, G. P., & von Clarmann, T. 2014, JGR, 119, 4429
Gao, P., Hu, R., Robinson, T. D., Li, C., & Yung, Y. L. 2015, ApJ, 806, 249
Gao, P., Zhang, X., Crisp, D., Bardeen, C. G., & Yung, Y. L. 2014, Icar, 231, 83
Gardner, J. P., Mather, J. C., Clampin, M., et al. 2006, Space Science Reviews, 123, 485
Gebauer, S., Grenfell, J., Lehmann, R., & Rauer, H. 2018a, AsBio, 18, 856
Gebauer, S., Grenfell, J. L., Lehmann, R., & Rauer, H. 2018b, ACS Earth and Space Chem., 2, 1112
Gierasch, P., & Conrath, B. 1985, Recent Advances in Planetary Meteorology, 121
Gillon, M., Jehin, E., Lederer, S. M., et al. 2016, Natur, 533, 221
Gillon, M., Triaud, A. H., Demory, B.-O., et al. 2017, Natur, 542, 456
Gillon, M., Meadows, V., Agol, E., et al. 2020, arXiv preprint arXiv:2002.04798
Gilmozzi, R., & Spyromilio, J. 2007, The Messenger, 127, 3
Giorgi, F., & Chameides, W. 1985, JGR: Atmospheres, 90, 7872
Godolt, M., Grenfell, J., Kitzmann, D., et al. 2016, A&A, 592, A36
Gordon, I., Rothman, L., Hill, C., et al. 2017, JQSRT, 203, 3
Grenfell, J., Gebauer, S., Godolt, M., et al. 2013, AsBio, 13, 415
Grenfell, J. L., Gebauer, S., Godolt, M., et al. 2018, ApJ, 861, 38
Grenfell, J. L., Gebauer, S., Paris, P. v., Godolt, M., & Rauer, H. 2014, P&SS, 98, 66
Grenfell, J. L., Stracke, B., von Paris, P., et al. 2007, P&SS, 55, 661
Grimm, S. L., Demory, B.-O., Gillon, M., et al. 2018, A&A, 613, A68
Gueymard, C. A. 2004, Solar energy, 76, 423
Guo, J. H. 2019, ApJ, 872, 99
Haberle, R. M., Clancy, R. T., Forget, F., Smith, M. D., & Zurek, R. W. 2017, The atmosphere and climate of Mars (Cambridge University Press)
Harman, C. E., Schwieterman, E. W., Schottelkotte, J. C., & Kasting, J. F. 2015, ApJ, 812, 137
Hartogh, P., Jarchow, C., Lellouch, E., et al. 2010, A&A, 521, L49
Hauglustaine, D., Granier, C., Brasseur, G., & Megie, G. 1994, JGR: Atmospheres, 99, 1173
Hauschildt, P. 1993, JQSRT, 50, 301
Hauschildt, P. H., & Baron, E. 2006, A&A, 451, 273

Hu, R., Peterson, L., & Wolf, E. T. 2020, ApJ, 888, 122
Hu, R., Seager, S., & Bains, W. 2012, ApJ, 761, 166
Huang, J., Huang, J., Liu, X., et al. 2018, Science bulletin, 63, 1180
Hunten, D. M. 1975, Proceedings of the National Academy of Sciences, 72, 4711
Izakov, M. 2001, P&SS, 49, 47
Johnstone, C. P. 2020, ApJ, 890, 79
Junge, C. 1952, Berichte des deutschen Wetterdienstes in der US-Zone, 35, 261
—. 1955, J. Meteorol., 12, 13
Kaltenegger, L., & Traub, W. A. 2009, ApJ, 698, 519
Kane, S. R. 2018, ApJ, 861, L21
Karman, T., Gordon, I. E., van der Avoird, A., et al. 2019, Icar, 328, 160
Kasting, J. F., & Ackerman, T. P. 1986, Science, 234, 1383
Kasting, J. F., Holland, H. D., & Pinto, J. P. 1985, JGR: Atmospheres, 90, 10497
Kasting, J. F., Whitmire, D. P., & Reynolds, R. T. 1993, Icar, 101, 108
Katyal, N., Nikolaou, A., Godolt, M., et al. 2019, ApJ, 875, 31
Keller-Rudek, H., Moortgat, G. K., Sander, R., & Sörensen, R. 2013, Earth System Science Data, 5, 365
Kendrew, S., Scheithauer, S., Bouchet, P., et al. 2015, PASP, 127, 623
Khalil, M., & Rasmussen, R. 1984, Atmospheric Environment (1967), 18, 1805
Kharecha, P., Kasting, J., & Siefert, J. 2005, Geobiology, 3, 53
Kitzmann, D., Patzer, A., von Paris, P., Godolt, M., & Rauer, H. 2011a, A&A, 531, A62
—. 2011b, A&A, 534, A63
Kitzmann, D., Patzer, A., von Paris, P., et al. 2010, A&A, 511, A66
Kleinböhl, A., Schofield, J. T., Kass, D. M., et al. 2009, JGR: Planets, 114
Komacek, T. D., Fauchez, T. J., Wolf, E. T., & Abbot, D. S. 2020, ApJ, 888, L20
Krasnopolsky, V. A. 2006, Icar, 182, 80
—. 2007, Icar, 191, 25
—. 2010a, Icar, 207, 638
—. 2010b, Icar, 209, 314
—. 2012, Icar, 218, 230
—. 2017, P&SS, 144, 71
Krasnopolsky, V. A., & Feldman, P. D. 2001, Science, 294, 1914
Krissansen-Totton, J., Garland, R., Irwin, P., & Catling, D. C. 2018a, AJ, 156, 114
Krissansen-Totton, J., Olson, S., & Catling, D. C. 2018b, Science advances, 4, eaao5747
Kritz, M. A., & Rancher, J. 1980, JGR: Oceans, 85, 1633
Krivolutsky, A. 2001, Advances in Space Research, 27, 1993
Kump, L. R. 2008, Nature, 451, 277
Lebonnois, S., Quémerais, E., Montmessin, F., et al. 2006, JGR: Planets, 111
Leconte, J., Wu, H., Menou, K., & Murray, N. 2015, Science, 347, 632
Legrand, M., Preunkert, S., Wagenbach, D., & Fischer, H. 2002, JGR: Atmospheres, 107, ACH
Lelieveld, J., Crutzen, P. J., & Dentener, F. J. 1998, Tellus B, 50, 128
Lincowski, A. P., Meadows, V. S., Crisp, D., et al. 2018, ApJ, 867, 76
Liske, J. 2008, E-ELT Spectroscopic ETC: Detailed Description, Tech. rep., Technical Report
Loftus, K., Wordsworth, R. D., & Morley, C. V. 2019, ApJ, 887, 231
López-Morales, M., Ben-Ami, S., Gonzalez-Abad, G., et al. 2019, AJ, 158, 24
López-Puertas, M., Funke, B., Gil-López, S., et al. 2005, JGR: Space Physics, 110
López-Puertas, M., García-Comas, M., Funke, B., et al. 2018, Atmospheric Measurement Techniques, 11, 2187
Lu, H.-C., Chen, H.-K., Chen, H.-F., Cheng, B.-M., & Ogilvie, J. 2010, A&A, 520, A19
Luger, R., & Barnes, R. 2015, AsBio, 15, 119
Lustig-Yaeger, J., Meadows, V. S., & Lincowski, A. P. 2019, AJ, 158, 27
Madhusudhan, N., & Redfield, S. 2015, International Journal of Astrobiology, 14, 177189
Mallard, W., Westley, F., Herron, J., Hampson, R., & Frizzell, D. 1994, National Institute of Standards and Technology, Gaithersburg, MD
Manabe, S., & Wetherald, R. T. 1967, JAS, 24, 241
Manatt, S. L., & Lane, A. L. 1993, JQSRT, 50, 267
Marconi, A., Di Marcantonio, P., D'Odorico, V., et al. 2016, Proc. SPIE, 9908, 990823
Marcq, E., Belyaev, D., Montmessin, F., et al. 2011, Icar, 211, 58
Marrero, T. R., & Mason, E. A. 1972, Journal of Physical and Chemical Reference Data, 1, 3
Mason, N. J., Gingell, J. M., Davies, J. A., et al. 1996, Journal of Physics B: Atomic, Molecular and Optical Physics, 29, 3075
Massie, S., & Hunten, D. 1981, JGR: Oceans, 86, 9859
Meadows, V. S. 2017, AsBio, 17, 1022
Mennesson, B., Gaudi, S., Seager, S., et al. 2016, Proc. SPIE, 9904, 99040L

Mills, F. P. 1998, PhD thesis, California Institute of Technology
Mills, F. P., & Allen, M. 2007, P&SS, 55, 1729
Minschwaner, K., Anderson, G. P., Hall, L. A., & Yoshino, K. 1992, JGR, 97, 10103
Mlawer, E. J., Payne, V. H., Moncet, J.-L., et al. 2012, Philosophical Transactions of the Royal Society A: Mathematical, Physical and Engineering Sciences, 370, 2520
Mollière, P., & Snellen, I. 2019, A&A, 622, A139
Montmessin, F., & Ferron, S. 2019, Icar, 317, 549
Montmessin, F., & Lefèvre, F. 2013, Nature Geoscience, 6, 930
Montmessin, F., Korablev, O., Lefèvre, F., et al. 2017, Icar, 297, 195
Moran, S. E., Hörst, S. M., Batalha, N. E., Lewis, N. K., & Wakeford, H. R. 2018, AJ, 156, 252
Morley, C. V., Kreidberg, L., Rustamkulov, Z., Robinson, T., & Fortney, J. J. 2017, ApJ, 850, 121
Moses, J. I., Visscher, C., Fortney, J. J., et al. 2011, The Astrophysical Journal, 737, 15
Murphy, W. F. 1977, The Journal of Chemical Physics, 67, 5877
Nair, H., Allen, M., Anbar, A. D., Yung, Y. L., & Clancy, R. T. 1994, Icar, 111, 124
Nava-Sedeño, J. M., Ortiz-Cervantes, A., Segura, A., & Domagal-Goldman, S. D. 2016, AsBio, 16, 744
Nelson, J., & Sanders, G. H. 2008, Proc. SPIE, 7012, 70121A
Nowlan, C. R., Martin, R. V., Philip, S., et al. 2014, Global Biogeochemical Cycles, 28, 1025
O'Malley-James, J. T., & Kaltenegger, L. 2017, MNRAS Letters, 469, L26
—. 2019, MNRAS, 485, 5598
Origlia, L., Oliva, E., Maiolino, R., et al. 2010, Proc. SPIE, 7735, 77352B
Owen, T., Biemann, K., Rushneck, D., et al. 1977, JGR, 82, 4635
Pavlov, A. A., & Kasting, J. 2002, AsBio, 2, 27
Pavlov, A. A., Kasting, J. F., Brown, L. L., Rages, K. A., & Freedman, R. 2000, JGR: Planets, 105, 11981
Peacock, S., Barman, T., Shkolnik, E. L., Hauschildt, P. H., & Baron, E. 2019, ApJ, 871, 235
Phillips, S. B., Arya, S. P., & Aneja, V. P. 2004, Atmospheric Environment, 38, 3469
Pidhorodetska, D., Fauchez, T., Villanueva, G., & Domagal-Goldman, S. 2020, arXiv preprint arXiv:2001.01338
Prather, M., Derwent, R., Ehhalt, D., et al. 1995, IPCC Report 1994
Pyle, D., & Mather, T. 2009, Chemical Geology, 263, 110
Ramirez, R. M., & Kaltenegger, L. 2014, ApJL, 797, L25
Rauer, H., Gebauer, S., von Paris, P., et al. 2011, A&A, 529, A8
Rodler, F., & López-Morales, M. 2014, ApJ, 781, 54
Rugheimer, S., Kaltenegger, L., Segura, A., Linsky, J., & Mohanty, S. 2015, ApJ, 809, 57
Ryan, S., Dlugokencky, E. J., Tans, P. P., & Trudeau, M. E. 2006, Geophys. Res. Lett., 33
Sánchez-López, A., Alonso-Floriano, F., López-Puertas, M., et al. 2019, A&A, 630, A53
Sander, R. 2015, Atmospheric Chemistry & Physics, 15
Sander, S., Friedl, R., Abbatt, J., et al. 2011, JPL publication, 10
Sandor, B. J., & Clancy, R. T. 2012, Icar, 220, 618
Sandor, B. J., Clancy, R. T., Moriarty-Schieven, G., & Mills, F. P. 2010, Icar, 208, 49
Sanhueza, E., Dong, Y., Scharffe, D., Lobert, J., & Crutzen, P. 1998, Tellus B: Chemical and Physical Meteorology, 50, 51
Schaefer, L., Wordsworth, R. D., Berta-Thompson, Z., & Sasselov, D. 2016, ApJ, 829, 63
Scheucher, M., Grenfell, L., Wunderlich, F., et al. 2018, ApJ, 863
Scheucher, M., Wunderlich, F., Grenfell, J. L., et al. accepted, ApJ
Scheucher, M., Herbst, K., Schmidt, V., et al. 2020, ApJ
Schreier, F., Gimeno García, S., Hedelt, P., et al. 2014, JQSRT, 137, 29
Schreier, F., Städt, S., Hedelt, P., & Godolt, M. 2018, Molecular Astrophysics, 11, 1
Schwieterman, E. W., Reinhard, C. T., Olson, S. L., et al. 2019, ApJ, 874, 9
Segura, A., Kasting, J. F., Meadows, V., et al. 2005, AsBio, 5, 706
Segura, A., Krelove, K., Kasting, J. F., et al. 2003, AsBio, 3, 689
Segura, A., Meadows, V., Kasting, J., Crisp, D., & Cohen, M. 2007, A&A, 472, 665
Sehmel, G. A. 1980, Atmospheric Environment (1967), 14, 983
Seiff, A., Schofield, J., Kliore, A., et al. 1985, Advances in Space Research, 5, 3
Seinfeld, J. H., & Pandis, S. N. 2016, Atmospheric chemistry and physics: from air pollution to climate change (John Wiley & Sons)
Selsis, F., Despois, D., & Parisot, J.-P. 2002, A&A, 388, 985
Selwyn, G., Podolske, J., & Johnston, H. S. 1977, Geophys. Res. Lett., 4, 427

Serdyuchenko, A., Gorshelev, V., Weber, M., Chehade, W., & Burrows, J. P. 2014, Atmospheric Measurement Techniques, 7, 625
Serindag, D. B., & Snellen, I. A. G. 2019, ApJ, 871, L7
Shardanand, & Rao, A. D. P. 1977, Absolute Rayleigh scattering cross sections of gases and freons of stratospheric interest in the visible and ultraviolet regions
Sheese, P. E., Boone, C. D., & Walker, K. A. 2015, Atmospheric Measurement Techniques, 8, 741
Siskind, D. E., Nedoluha, G. E., Randall, C. E., Fromm, M., & Russell III, J. M. 2000, Geophys. Res. Lett., 27, 329
Sneep, M., & Ubachs, W. 2005, JQSRT, 92, 293
Snellen, I., de Kok, R., Birkby, J., et al. 2015, A&A, 576, A59
Snellen, I. A. G., de Kok, R. J., le Poole, R., Brogi, M., & Birkby, J. 2013, ApJ, 764, 182
Stark, C. C., Roberge, A., Mandell, A., et al. 2015, ApJ, 808, 149
Suissa, G., Mandell, A. M., Wolf, E. T., et al. 2020, ApJ, 891, 58
Svedhem, H., Titov, D. V., Taylor, F. W., & Witasse, O. 2007, Natur, 450, 629
Tabataba-Vakili, F., Grenfell, J., Grießmeier, J.-M., & Rauer, H. 2016, A&A, 585, A96
The LUVOIR Team. 2019, arXiv preprint arXiv:1912.06219
Tian, F. 2015, EPSL, 432, 126
Tian, F., France, K., Linsky, J. L., Mauas, P. J., & Vieytes, M. C. 2014, EPSL, 385, 22
Tian, F., & Ida, S. 2015, Nature Geoscience, 8, 177
Tie, X., Guenther, A., & Holland, E. 2003, Geophys. Res. Lett., 30
Toon, O. B., McKay, C., Ackerman, T., & Santhanam, K. 1989, JGR, 94, 16287
Toon, O. B., & Pollack, J. B. 1976, Journal of Applied Meteorology, 15, 225
Trainer, M. G., Wong, M. H., McConnochie, T. H., et al. 2019, JGR: Planets, 124, 3000
Tsiaras, A., Waldmann, I. P., Tinetti, G., Tennyson, J., & Yurchenko, S. N. 2019, Nat. Astron., 1
Turbet, M., Ehrenreich, D., Lovis, C., Bolmont, E., & Fauchez, T. 2019, A&A, 628, A12
Turbet, M., Bolmont, E., Leconte, J., et al. 2018, A&A, 612, A86
Van Grootel, V., Fernandes, C. S., Gillon, M., et al. 2018, ApJ, 853, 30
Vandaele, A., Korablev, O., Belyaev, D., et al. 2017, Icar, 295, 16
Vandaele, A. C., Korablev, O., Daerden, F., et al. 2019, Natur, 568, 521
Vasquez, M., Schreier, F., Gimeno García, S., et al. 2013, A&A, 557, A46
von Clarmann, T., Höpfner, M., Kellmann, S., et al. 2009, Atmospheric Measurement Techniques, 2, 159
von Paris, P., Cabrera, J., Godolt, M., et al. 2011, A&A, 534, A26
von Paris, P., Rauer, H., Grenfell, J. L., et al. 2008, P&SS, 56, 1244
von Paris, P., Selsis, F., Godolt, M., et al. 2015, Icar, 257, 406
von Paris, P., Gebauer, S., Godolt, M., et al. 2010, A&A, 522, A23
Wakeford, H. R., Lewis, N. K., Fowler, J., et al. 2018, AJ, 157, 11
Wang, Y., Tian, F., Li, T., & Hu, Y. 2016, Icar, 266, 15
Watson, R. 1992, The IPCC Scientific Assessment.
Webster, C. R., Mahaffy, P. R., Atreya, S. K., et al. 2018, Science, 360, 1093
Williams, D. 2010, Mars Fact Sheet. National Space Science Data Center. NASA
Wilson, D. J., Froning, C. S., Duvvuri, G. M., et al. submitted, ApJ
Wofsy, S. C., McConnell, J. C., & McElroy, M. B. 1972, JGR, 77, 4477
Wolf, E. T. 2017, ApJL, 839, L1
Wordsworth, R., & Pierrehumbert, R. 2014, ApJ, 785, L20
Wordsworth, R. D., & Pierrehumbert, R. T. 2013, ApJ, 778, 154
Wordsworth, R. D., Schaefer, L. K., & Fischer, R. A. 2018, AJ, 155, 195
Wright, S. A., Larkin, J. E., Moore, A. M., et al. 2014, Proc. SPIE, 9147, 3208
Wunderlich, F., Godolt, M., Grenfell, J. L., et al. 2019, A&A, 624, A49
Yan, F., Fosbury, R. A., Petr-Gotzens, M. G., et al. 2015, IJA, 14, 255
Yang, J., Cowan, N. B., & Abbot, D. S. 2013, ApJL, 771, L45
Yoshino, K., Parkinson, W., Ito, K., & Matsui, T. 2005, J. Mol. Spectrosc., 229, 238
Zahnle, K., Haberle, R. M., Catling, D. C., & Kasting, J. F. 2008, JGR: Planets, 113
Zhang, X., Liang, M. C., Mills, F. P., Belyaev, D. A., & Yung, Y. L. 2012, Icar, 217, 714
Zhang, X., & Showman, A. P. 2018, ApJ, 866, 1